Computers and Structures 257 (2021) 106645

Contents lists available at ScienceDirect

Computers and Structures

journal homepage: www.elsevier.com/locate/compstruc

A continuous energy-based numerical approach to predict fracture mechanisms in masonry structures: CDF method

A. Iannuzzo [a], P. Block [a], M. Angelillo [b], A. Gesualdo [c,*]

[a] ETH Zurich, Institute of Technology in Architecture, Block Research Group, Stefano-Franscini-Platz 1, HIB E45, CH-8093 Zurich, Switzerland
[b] Department of Civil Engineering, University of Salerno, Salerno, Italy
[c] Department of Structures for Engineering and Architecture, University of Naples Federico II, Napoli, Italy

ARTICLE INFO

Article history:
Received 23 October 2020
Accepted 20 July 2021
Available online xxxx

Keywords:
Masonry
No-tension material
Settlements
Smeared Cracks
Continuous Displacement for Fracture (CDF) method

ABSTRACT

In the present paper, we propose the Continuous Displacement for Fracture (CDF) method, a continuous energy-based numerical approach to find mechanisms and crack patterns exhibited by 2D masonry structures subjected to given loads and settlements. The structure is modelled through the normal, rigid, no-tension material, and the equilibrium problem is solved as the minimum of the total potential energy (TPE). With the CDF method the solution is sought in the space of continuous functions. The CDF performances are compared and illustrated against the PRD approach that finds the TPE minimum in the space of small, piecewise-rigid displacements.

The CDF method is displacement-based approach, allowing for a direct control of the effects of foundation settlements. Some problems are proposed to benchmark the methodology against both PRD and analytical solutions to also clearly illustrate its peculiarities. Finally, its use and potentials are benchmarked and compared on a case study. CDF provides results in good agreement with both the PRD approach and another more sophisticated model. The main outcome is that, although more computationally cumbersome, CDF is mesh independent and perfectly captures a clear subdivision of the structural domain into macro-regions behaving as rigid or quasi-rigid bodies.

1. Introduction

The present paper focuses on the prediction of the fracture mechanisms exhibited by masonry constructions subjected to given load and kinematical data (i.e. settlements/distortions). Most part of the building heritage all over the world is represented by masonry structures. Although they represent the most ancient and durable technology for housing or monumental buildings, their mechanical behaviour is currently subjected to an in-deep scientific investigation whose aim is to predict the mechanical response to different actions and, consequently, to preserve them as a clear manifestation of cultural heritage for the next generations.

Accurate numerical strategies have been developed in recent years to assess masonry structures using completely different methods: non-associative, limit analysis-based approaches [1,2,3,4,5,6], finite element method [7,8,9,10] and, recently, distinct element method [11,12,13,14,15,16,17,18,19]. Nonetheless, in the current scientific field, the correct modelling of the effects of settlements on masonry structures is a critical issue and still a cutting edge, open topic.

Indeed, settlements and distortions are the most elusive data for the constructions of Civil Engineering. However, structures subject to internal and external unilateral constraints, such as the masonry ones, are less critically sensitive to this issue rather than over-determined structures subject to bilateral constraints (e.g. steel and reinforced concrete structures). For detailed info concerning unilateral constraints, the reader is referred to [20]. Structures under unilateral constraints can indeed, at the same time, be statically overdetermined and admit zero-energy modes, thus naturally and smoothly accommodating the effect of kinematical data. Indeed, the effect of settlements on a structure made up of stones or of masonry is often represented by a simple mechanism involving a finite number of rigid blocks [21]. The first who noticed this peculiar behaviour was Danyzy in 1732 [22] with some tests reported by Frézier [23]. In recent years, many scholars have proposed different strategies to predict the effect and assess the stability of masonry undergoing foundation displacements, as in [24,25,26,27,28,29,30]. Although the prediction of the effects of given foundation displacements is a complex topic, identifying

* Corresponding author.
E-mail addresses: iannuzzo@arch.ethz.ch (A. Iannuzzo), block@arch.ethz.ch (P. Block), mangelillo@unisa.it (M. Angelillo), gesualdo@unina.it (A. Gesualdo).

https://doi.org/10.1016/j.compstruc.2021.106645
0045-7949/

the exact foundation displacement profile producing an observed crack pattern represents an even higher computational task. Indeed, such an inverse-analysis, requiring a large number of different evaluations, is facilitated by tools allowing fast computational solving and whose results are as less as possible sensitive to the values of the mechanical parameters.

With this in mind, in the present paper, we introduce and illustrate a new energy-based continuous approach to predict crack patterns due to settlements. The masonry material is modelled through the simplified model of Heyman [31], which can be extended to continuum masonry structures on adopting the normal, rigid, no-tension (NRNT) material [32]. For NRNT continua, the theorems of Limit Analysis are still valid as first shown by Kooharian [33] and proved by Heyman [31]. Since then, many papers proposing applications of Limit Analysis to masonry structures have appeared in the literature. Amongst them we recall the work by Como [34], and more recently by Angelillo [32,35,36], Angelillo et al [37,38,39], Block [40], Block et al [41,42,43], Coccia [44,45], Fortunato et al [46], Gesualdo et al [47,48], Huerta [49,50,51], Ochsendorf [52,53], Oliveri et al. [91], and Zampieri [54].

The NRNT material is the most simplified model that can be adopted to represent masonry structure mechanics. It does not depend on any mechanical parameter as it is perfectly rigid in compression and soft in tension. Nonetheless, the crude but stringent Heyman's material allows catching the essence of the behaviour of most traditional masonry structures, at least of those having the minimal quality of masonry [55] and subjected to a low-stress level. However, the NRNT model does not catch sophisticated features such as elastic–plastic interactions, crushing, hysteresis, damage and degradation (though these might be added by refining the model, at the price of losing linearity). Moreover, for highly stressed constructions, more correct simulation of the sliding, shear-type behaviour can be accomplished by adding to the NRNT model a limit on compressive stresses [56,57,58], and introducing a flow rule for the corresponding inelastic strain rates. Additionally, for frictional and cohesive-less contact behaviour of the masonry material modelled using rigid blocks the reader is referred to [1,2,3,30].

By adopting the NRNT model for the material and using a displacement approach, we propose a minimum-energy criterion to look for solutions of typical mixed boundary value problem (BVP) for NRNT structures. Specifically, the energy criterion is based on the minimum of the total potential energy (TPE), that was first introduced to solve typical masonry mechanics problems in [59,60] and later on also explored in [61,62] where the internal dissipation over the interfaces were modelled assuming classic limit analysis yield surfaces. In more sophisticated models for brittle materials, the energy is the sum of the potential energy of the applied loads and of the elastic (bulk) and interface (surface) ones, the latter being the energy expended to activate a crack system on a set of internal surfaces [63,64,65]. With the NRNT material, the energy reduces to the potential energy of the external loads solely [66]. Therefore, neglecting the elastic and interface energy, the criterion we adopt is based on the minimisation of the total potential energy of the external loads only.

The proposed minimum energy criterion [59] constitutes an efficient orientation to model a wide range of masonry structures as an alternative to more sophisticated numerical models [67,68,69] requiring costly and often unfeasible experiments to calibrate many numerical parameters and all too often needing a precise knowledge of the construction details and loading histories. Particularly, the key point of the proposed approaches lies in the absence of any mechanical parameter and, most importantly, in the direct use of a displacement-based approach, more appropriate when the aim is to handle as primal variable the displacements to better model the fracture pattern effects due to non-homogeneous kinematical boundary conditions.

A key aspect of the use of the NRNT material comes from the possibility of taking into account both singular and continuous strain and stress fields, even simultaneously.

To clearly and robustly highlight this aspect, a new continuous numerical method to approximate the solution of the TPE-minimum is proposed, illustrated and compared against analytical solutions and other models clarifying its pros and cons. This method, named Continuous Displacement for Fracture (CDF), throughout the paper, is compared against the Piecewise Rigid Displacement (PRD) method [70,71]. While with the PRD method, the energy is minimized within the set of piecewise-rigid displacements and the strains are purely singular, with the CDF method, the search for the minimum is restricted to continuous displacement fields, for which the strain is purely regular. The PRD structural discretisation entails a subdivision of the structural domain, which can be thought of as an assembly of rigid blocks where fractures can appear on the interface amongst blocks as *concentrated cracks*. Conversely, the CDF approach is based on a classical finite element (FE) mesh description of the structural domain where the nodal displacements are continuous. In this case, the strain cannot be singular, and fractures appear as *smeared*, even if narrow bands (which may even cross single elements) where high strains are present may be detected. The PRD approach has been successfully developed and pushed forward in the last years, even though its numerical peculiarities for fully 2D elements (such as complex wall systems with openings) has not been completely explored yet. To this aim, this paper aims at also proposing a critical theoretical study and comparison of these two opposite approaches also to show how the NRNT material model provides in two different ways a good mechanical description of the response of masonry structures subjected to foundation displacements. We have to point out that, even though here these two approaches are conceived and illustrated with respect to settlement problems, they can be applied to also solve other practical assessment problems, such as load-bearing capacity or seismic stability analyses. However, these last aspects are outside the scope of the present paper.

We will illustrate that the NRNT model, though representing a crude approximation of the material behaviour, describes the most relevant peculiarity of masonry, that is, the formation of rigid macroblock regions, which is the preferred failure mode for real masonry structures when subject to settlements (Fig. 1) or when shaken by severe earthquakes. Nonetheless, this phenomenological aspect stems from mechanical characteristics, such as toughness and cohesion, which are not strictly inherent to the simplified NRNT continuum model. So, it is interesting to see if rigid block mechanisms can arise naturally in solving the minimum problem, or if there is any legitimate way to force rigid block mechanisms over diffuse cracking to catch that behaviour. Indeed, the main motivation for using the PRD approximation lies in the fact that real masonry structures exhibit such rigid block mechanisms, when subject to settlements (Fig. 1) or to horizontal accelerations due to earthquakes. And, in this sense, the PRD approach provides a good starting modelling point as it assumes a priori the piecewise rigidity of the domain. Conversely, with the CDF method, we explore the possibility to catch this physical behaviour by restricting the minimum-energy search to continuous displacement fields. However, simply using the CDF method does not automatically and always guarantee a rigid macroblock partition of the domain as a solution of the minimum problem. Indeed, as noted, bands of concentrated strains representing smeared cracks are allowed. We will clearly show how providing the CDF method with the so-called **Safe Load Condition** [72,73] a clear macroblock subdivision of the structural domain can be captured regardless of the mesh

Fig. 1. The effect of soil settlements on the Deba bridge (Spain): a clear subdivision of the structural domain into rigid macroblocks can be seen.

adopted. Indeed, although computationally more cumbersome, the key aspect in using the CDF approach is its mesh independence.

After briefly recalling the basic ingredients of PRD, the CDF method is introduced. Some benchmark problems of increasing complexity are proposed to compare the CDF approach against both the PRD method and analytical solutions to clearly illustrate its pros and cons. Finally, we benchmark the CDF approach on a masonry façade analysed through a normal, elastic, no-tension model in [57] to show and discuss their potentials and numerical performances on a real case study, especially with respect to the mesh-dependency issue.

2. Framing Heyman's model into continuum mechanics

A 2D masonry structure is modelled as a continuum occupying the region Ω of the Euclidean space $\mathscr{E}^2$. The stress tensor is denoted $\mathbf{T}$ and the displacement of material points $\mathbf{x}$ belonging to Ω as $\mathbf{u}$. On adopting the small displacements assumption, the infinitesimal strain tensor $\mathbf{E}$ is assumed as the measure of the deformation. Let $\mathbf{b}$ represent the body forces on Ω, $\mathbf{n}$ the unit, outward normal to the boundary $\partial\Omega$ which is partitioned into its constrained part $\partial\Omega_D$, where given displacement $\bar{\mathbf{u}}$ are prescribed, and in its loaded part $\partial\Omega_N$, on which surface tractions $\bar{\mathbf{s}}$ [74] are prescribed (see Fig. 2). Moreover, in what follows we extensively use the term latent strain, meaning the inelastic deformation needed to sustain the unilateral constraint on stress.

2.1. The NRNT material

The Heyman model can be generalized to 2D continua by introducing unilateral material restrictions on the stress and convenient assumptions on the corresponding latent strain. The normal, rigid, no-tension (NRNT) material is defined by the following restrictions:

$$\mathbf{T} \in \mathrm{Sym}^- \ , \ \mathbf{E} \in \mathrm{Sym}^+ \ , \ \mathbf{T}\cdot\mathbf{E} = 0, \tag{1}$$

in which Sym^-, Sym^+ are the mutually polar cones of negative and positive semidefinite symmetric tensors. Restrictions (1) are equivalent to the following conditions, called normality conditions:

$$\mathbf{T} \in \mathrm{Sym}^- \ , \ (\mathbf{T}-\mathbf{T}^*)\cdot\mathbf{E} \geq 0 \ , \ \forall\, \mathbf{T}^* \in \mathrm{Sym}^-, \tag{2}$$

and, dually, to the so-called dual normality conditions:

$$\mathbf{E} \in \mathrm{Sym}^+ \ , \ (\mathbf{E}-\mathbf{E}^*)\cdot\mathbf{T} \geq 0 \ , \ \forall\, \mathbf{E}^* \in \mathrm{Sym}^+. \tag{3}$$

The restrictions defining the NRNT material, in the particular form (2), are the essential ingredients for the validity of the theorems of Limit Analysis [33,72,68,75]. The mathematics of unilateral materials is rich and complex, since the inherent ambient function spaces for NRNT materials are not classical Sobolev spaces. Nonetheless, for such materials, one can admit that strain and stress are bounded measures [76]. Therefore, they can be additively decomposed into the sum of regular $(.)^r$ and singular $(.)^s$ parts, namely:

$$\mathbf{E} = \mathbf{E}^r + \mathbf{E}^s \ , \ \mathbf{T} = \mathbf{T}^r + \mathbf{T}^s, \tag{4}$$

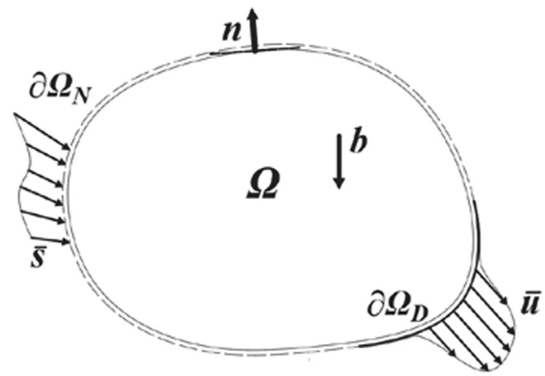

Fig. 2. A 2D continuum occupying a region Ω of the Euclidean space. Load tractions on $\partial\Omega_N$ are represented by $\bar{\mathbf{s}}$ whilst prescribed boundary displacement on $\partial\Omega_D$ by $\bar{\mathbf{u}}$.

where the regular part $(.)^r$ is absolutely continuous with respect to the area measure, that is, is a density per unit area, and $(.)^s$ is the singular part. Typical singular strains are the line Dirac deltas, which, in the case of strain, represent the effect of displacement jumps (concentrated cracks) and, in the case of stress, the effect of some kind of jumps of the stress vector (concentrated axial forces). Indeed, on admitting singular strains and stresses, it is possible to consider that both the displacement $\mathbf{u}$ and the stress vector $\mathbf{s}$ can be discontinuous. The stress vector is defined as the contact force transmitted across any internal surface of unit normal $\mathbf{n}$, and, in Cauchy's sense, is related to the regular part of the stress through the relation $\mathbf{s} = \mathbf{T}^r\mathbf{n}$. The jump of $\mathbf{s}$ across a regular curve can be balanced by singular stresses $\mathbf{T}^s$ concentrated on the jump curve. Crushing phenomena or workmanship of bad quality that can produce disarrangements in the block pattern [77], can be modelled as eigenstrains $\bar{\mathbf{E}}$, and even them can be singular, and denoted $\bar{\mathbf{E}}^s$.

2.2. The boundary value problem

The equilibrium of a 2D masonry structure, modelled as a continuum composed of NRNT material subjected to loads and settlements, can be formulated as a boundary value problem (BVP), in the following form. "*Find a displacement field* $\mathbf{u}$ *and the corresponding strain* $\mathbf{E}$*, and a stress field* $\mathbf{T}$ *such that*

$$\mathbf{E} = \frac{1}{2}\left(\nabla\mathbf{u} + \nabla\mathbf{u}^T\right) \ , \ \mathbf{E} \in \mathrm{Sym}^+ \ , \ \mathbf{u} = \bar{\mathbf{u}} \text{ on } \ \partial\Omega_D, \tag{5}$$

$$\mathrm{div}\mathbf{T} + \mathbf{b} = 0 \ , \ \mathbf{T} \in \mathrm{Sym}^- \ , \ \mathbf{T}\mathbf{n} = \bar{\mathbf{s}} \text{ on } \ \partial\Omega_N, \tag{6}$$

$$\mathbf{T}\cdot\mathbf{E} = 0,\text{''} \tag{7}$$

$\mathbf{b}$ being the body forces and $\mathbf{n}$ the unit, outward normal to the boundary $\partial\Omega$ partitioned into its constrained part $\partial\Omega_D$ (on which the displacement $\bar{\mathbf{u}}$ are given), and in its loaded part $\partial\Omega_N$ (where the surface tractions $\bar{\mathbf{s}}$ are prescribed) [74].

On introducing the set $\mathscr{K}$ of kinematically admissible displacements, and the set $\mathscr{H}$ of statically admissible stresses

$$\mathscr{K} = \left\{ \mathbf{u} \in \mathrm{S} \;/\; \mathbf{E} = \frac{1}{2}(\nabla\mathbf{u} + \nabla\mathbf{u}^{\mathrm{T}}) \in \mathrm{Sym}^{+} \;\&\; \mathbf{u} = \bar{\mathbf{u}} \quad \text{on} \quad \partial\Omega_{\mathrm{D}} \right\}, \tag{8}$$

$$\mathscr{H} = \left\{ \mathbf{T} \in \mathrm{S}' \;/\; \mathrm{div}\mathbf{T} + \mathbf{b} = 0 \;,\; \mathbf{T} \in \mathrm{Sym}^{-} \;,\; \mathbf{T}\mathbf{n} = \bar{\mathbf{s}} \quad \text{on} \quad \partial\Omega_{\mathrm{N}} \right\}, \tag{9}$$

a solution of the BVP for masonry-like structures can be defined as a triplet $(\mathbf{u}^{\circ}, \mathbf{E}(\mathbf{u}^{\circ}), \mathbf{T}^{\circ})$ such that $\mathbf{u}^{\circ} \in \mathscr{K}$, $\mathbf{T}^{\circ} \in \mathscr{H}$, and $\mathbf{T}^{\circ} \cdot \mathbf{E}(\mathbf{u}^{\circ}) = 0$. It is worth noting that in Eqs. (8, 9) S, S' are two suitable function spaces which are not classical Sobolev spaces.

Remark 1. *The key peculiarity of NRNT materials is that they allow discontinuities both in the displacement vector field and in the stress vector field. Specifically, this model allows describing concentrated fractures as singular strains produced by displacement discontinuities and to consider singular, compressive, uniaxial stresses within the structural domain whose traces at the boundary are concentrated compressive forces (of any slope). Particularly, whenever we model internal stress states through lines of thrust [78] or thrust networks [42], we are implicitly assuming singular stress fields. In any case, such singular stress and strain fields can be seen as test functions needed to define the admissible solution sets. Predicting the real stress/strain state in detail is a difficult, and sometimes impossible, goal for most buildings. In the present context, as in the Limit Analysis spirit, we use admissible stress and strain fields to verify the possibility of equilibrium and to detect possible mechanisms* ■

3. Two numerical, energy-based strategies to approximate the solution of the BVP

Solving the BVP through a displacement approach consists in the search for a displacement field $\mathbf{u} \in \mathscr{K}$ for which there exists a stress field $\mathbf{T} \in \mathscr{H}$ such that $\mathbf{T} \cdot \mathbf{E}(\mathbf{u}) = 0$. Therefore, the way we use to find a displacement-based solution of the BVP is to minimise the potential energy $\wp(\mathbf{u})$, that is:

$$\wp(\mathbf{u}^{\circ}) = \min_{\mathbf{u} \in \mathscr{K}} \wp(\mathbf{u}). \tag{10}$$

For the NRNT material, $\wp(\mathbf{u})$ reduces to the potential energy of the external loads, and assuming small displacements and strains, it is a linear functional of $\mathbf{u}$. It is worth to point out that $\mathbf{u}^{\circ}$, i.e. the minimiser of $\wp(\mathbf{u})$, is the BVP solution for NRNT materials, and that its existence also guarantees the equilibrium of the loads imposed on the structure. If the kinematical problem is compatible (i.e. if the space $\mathscr{K}$ is not void), two results can be easily proved [59], namely:

i. if the load is compatible ($\mathscr{H} \neq \emptyset$) the linear functional $\wp(\mathbf{u})$ is bounded from below; and,
ii. a solution $(\mathbf{u}^{\circ}, \mathbf{E}(\mathbf{u}^{\circ}), \mathbf{T}^{\circ})$ of the BVP corresponds to a weak minimum of the $\wp(\mathbf{u})$.

Proving the sufficiency of condition (ii) under assumption (i), that is the existence of the minimum for the functional $\wp(\mathbf{u})$ in the function space setting described above, is a complicated mathematical task which exceeds the scopes of the present paper. So that we will heuristically accept the existence of the minimum.

In the next sections, we describe two different, displacement-based, numerical methods to find a solution of the minimum problem (10), namely the PRD method and the CDF method. With PRD, a method that was first introduced to solve typical masonry mechanics problems in [59,60], one assumes as set of kinematically admissible displacements the set $\mathscr{K}_{\mathrm{PRD}}$ of piecewise-rigid displacements, while with the second method, the search for a solution is restricted to continuous functions. Specifically, with the PRD method, the latent strain is purely singular, and the cracks forming in the structure are simulated by gap "openings" between adjacent rigid blocks. Conversely, the CDF method is based on an "opposite" idea, that is, the strain is assumed to be purely regular, and cracks appear as smeared. We will show how applying these two seemingly parallel numerical strategies to the same problems, we can catch the typical response of masonry, that is, we can predict the rigid macroblock partition of the structural domain.

3.1. Piecewise rigid displacement (PRD) method: Rigid blocks

In this section, the PRD method is recalled. It consists of finding an approximate solution of the problem (10) by restricting the minimum-search in the set $\mathscr{K}_{\mathrm{PRD}}$ of piecewise rigid displacements. $\mathscr{K}_{\mathrm{PRD}}$ is still an infinite-dimensional space and it is then discretised by considering a finite partition $(\Omega_{\mathrm{i}})_{\mathrm{i} \in \{1,2,..,\mathrm{M}\}}$, of the structural domain Ω into M rigid polygonal elements (Fig. 3). The boundary $\partial\Omega_{\mathrm{i}}$ of the n-polygon Ω_{i}, is composed of n segments Γ, of length ℓ, whose extremities are symbolically denoted 0,1 and whose unit normal and tangent vectors are $\mathbf{n}$, $\mathbf{t}$, respectively. We call interfaces the segments Γ that are, either the common boundaries between adjacent elements or part of the constrained boundary (i.e. those Γ representing interfaces with the soil or with other interacting structures). Let $\mathscr{K}^{\mathrm{M}}_{\mathrm{PRD}}$ be the finite dimensional approximation of $\mathscr{K}_{\mathrm{PRD}}$ generated by this partition. Therefore, the new, discretised, minimum-energy problem becomes:

$$\wp(\mathbf{u}^{\mathrm{o}}_{\mathrm{PRD}}) = \min_{\mathbf{u} \in \mathscr{K}^{\mathrm{M}}_{\mathrm{PRD}}} \wp(\mathbf{u}). \tag{11}$$

We can represent a generic piecewise rigid displacement $\mathbf{u} \in \mathscr{K}^{\mathrm{M}}_{\mathrm{PRD}}$ in terms of the vector $\mathbf{U}$ of 3M components representing the rigid body parameters of translation and rotation of the elements. Nevertheless, these parameters have to be constrained to fulfil the assumption that the strain must be positive semidefinite. For piecewise rigid displacements, the strain coincides with its singular part, namely:

$$\mathbf{E} = \mathbf{E}^{\mathrm{s}} = \mathrm{v}\;\delta(\Gamma)\;\mathbf{n} \otimes \mathbf{n} + \frac{1}{2}\mathrm{w}\;\delta(\Gamma)\;(\mathbf{t} \otimes \mathbf{n} + \mathbf{n} \otimes \mathbf{t}). \tag{12}$$

Within the present approximation, $\mathbf{E}^{\mathrm{s}}$ is concentrated along the interfaces among blocks, that is along the segments Γ. Material restrictions (2) can be translated as constraints on the displacement jumps, namely:

$$\mathrm{v} = [\mathbf{u}] \cdot \mathbf{n} \geq 0, \tag{13}$$

$$\mathrm{w} = [\mathbf{u}] \cdot \mathbf{t} = 0. \tag{14}$$

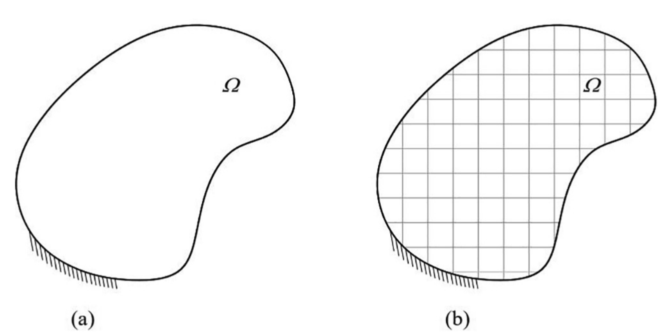

Fig. 3. The infinite-dimensional space $\mathscr{K}_{\mathrm{PRD}}$ of piecewise rigid displacement with support in the domain Ω represented in (a), is discretized considering a partition of the whole domain into convex polygonal elements: in (b) an example of the partition of the domain Ω with a grid of M elements is considered. The finite-dimensional approximation generated by this partition is $\mathscr{K}^{\mathrm{M}}_{\mathrm{PRD}}$.

Relations (13,14) ensure that tangential jumps (i.e. slidings) are not allowed while positive orthogonal jumps (i.e detachmenst) are admissible. Then the singular strain along the interface takes the form:

$$\mathbf{E} = \mathrm{v}\ \delta(\Gamma)\ \mathbf{n} \otimes \mathbf{n}. \tag{15}$$

Definitely, conditions (13) and (14), stemming from the assumption of normality, represent a condition of unilateral contact with no-sliding among blocks. It is to be pointed out that as we are looking at the incipient mechanism, the no-sliding condition represented by Eq. (14) has to be satisfied even the interface exhibit a normal detachment.

The static counterpart of these kinematical constraints concerns the stress vector $\mathbf{s}$ applied along Γ. Such a stress vector represents the reaction associated to the constraints (13,14). The stress vector $\mathbf{s}$ coincides with the given applied tractions $\bar{\mathbf{s}}$ where the boundary of the blocks becomes the loaded part of the boundary. With

$$\sigma = \mathbf{s} \cdot \mathbf{n}\ ,\ \ \tau = \mathbf{s} \cdot \mathbf{t}, \tag{16}$$

the normal σ and tangential τ stresses along Γ, the condition on $\mathbf{s}$ is

$$\sigma \leq 0. \tag{17}$$

Notice that the tangential component of $\mathbf{s}$ is not constrained and can be applied along the straight interface Γ, even if $\sigma = 0$. By calling N the total number of the interfaces Γ, and $\mathrm{v}(0), \mathrm{v}(1), \mathrm{w}(0), \mathrm{w}(1)$ the normal and tangential components of the relative displacements of the ends 0, 1 of any segment Γ, restrictions (12) and (13) are equivalent to the 2N inequalities

$$\mathrm{v}(0) \geq 0\ ,\ \ \mathrm{v}(1) \geq 0, \tag{18}$$

and the 2N equalities

$$\mathrm{w}(0) = 0\ ,\ \ \mathrm{w}(1) = 0. \tag{19}$$

Eqs. (14) and (19) model the no-sliding condition. In our opinion, shear cracks are important but not the most common in masonry structures [31,21]. Particularly, when the structure is subjected to foundation displacements, the more frequent are tensile cracks causing the formation of a rigid macroblock partition of the structure and thus relative movements between these parts. Furthermore, good masonry structures are constructed in such a way to avoid shearing as evil because of a good arrangement of the blocks as pointed out by Giuffré in [55]. Shear cracks can be sometimes seen locally either because of the bad masonry design or in panels where the crushing strength is locally exceeded. Restrictions (18), (19) can be easily expressed in terms of $\mathbf{U}$, in matrix forms:

$$\mathbb{A}_{\mathrm{ub}}\mathbf{U} \geq 0, \tag{20}$$

$$\mathbb{A}_{\mathrm{eq}}\mathbf{U} = 0. \tag{21}$$

where $\mathbb{A}_{\mathrm{u}}$ collects the unilateral restrictions and $\mathbb{A}_{\mathrm{e}}$ the no-sliding equations. The boundary conditions can be expressed as:

$$\mathbb{A}_{\mathrm{s,ub}}\mathbf{U} \geq \bar{\mathbf{U}}_{\mathrm{n}}\ ,\ \ \mathbb{A}_{\mathrm{s,eq}}\mathbf{U} = \bar{\mathbf{U}}_{\mathrm{t}}, \tag{22}$$

where matrices $\mathbb{A}_{\mathrm{s,ub}}$ and $\mathbb{A}_{\mathrm{s,eq}}$ enforce the prescribed displacements on the boundary. For more details, the reader is referred to [59,70]. Relations (20–22) define the set $\mathbb{K}^{\mathrm{M}}_{\mathrm{PRD}}$ of admissible displacement fields. The minimum problem (11) which approximates the minimum problem (10) is thus transformed into a linear programming problem:

$$\wp(\mathbf{U}^{\mathrm{o}}_{\mathrm{PRD}}) = \min_{\widehat{\mathbf{U}} \in \mathbb{K}^{\mathrm{M}}_{\mathrm{PRD}}} \wp(\mathbf{U}), \tag{23}$$

with:

$$\mathbb{K}^{\mathrm{M}}_{\mathrm{PRD}} = \left\{ \mathbf{U} \in \mathbb{R}^{3\mathrm{M}} / \mathbb{A}_{\mathrm{ub}}\mathbf{U} \geq 0, \mathbb{A}_{\mathrm{eq}}\mathbf{U} = 0, \mathbb{A}_{\mathrm{s,ub}}\mathbf{U} \geq \bar{\mathbf{U}}_{\mathrm{n}}, \mathbb{A}_{\mathrm{s,eq}}\mathbf{U} = \bar{\mathbf{U}}_{\mathrm{t}} \right\}. \tag{24}$$

Once the minimizer $\mathbf{U}^{\mathrm{o}}_{\mathrm{PRD}}$ has been obtained, one can easily construct the deformed configuration of the structure on which the relative displacements among the blocks play the role of fractures. Generally, the moving part can be idealised as a kinematical-chain controlled by the form of the given settlements and, in this sense, is statically determined.

The minimization problem (23) transforms the original continuum minimum problem (10) into a minimum problem for a structure composed of rigid parts, acted on by given loads and given settlements and subjected to unilateral contact conditions along the interfaces. Problem (23) is a standard linear finite-dimensional minimisation problem, since $\wp(\mathbf{U})$is a linear function of the 3M dimensional vector $\mathbf{U}$ and the constraints (24) are linear relations. The existence of the solution of this approximate problem is trivially guaranteed if the original problem is bounded from below. For a small number of variables, it can be solved exactly with the simplex method [79], and for large problems, there exist a number of well-known and efficient, approximate fast alternatives based on the interior-point algorithm [80,81,82].

It is worth pointing out that $\mathscr{K}_{\mathrm{PRD}}$ is a particular subspace of SBV functions [76]; its members are such that the corresponding strain is purely singular. The singular strain is a concentrated strain in the form of a set of line Dirac delta functions defined over the skeleton of the mesh. Therefore, the crack pattern is identified by the set composed by the interfaces having non-zero singular strains, that is, by gap "openings" between adjacent rigid blocks in the deformed configuration

3.2. Continuous displacement for fracture (CDF)

In this section, the CDF method is introduced. With this method, based on an entirely different numerical strategy, the solution of the minimum problem (10) is approximated by restricting the search to the set of continuous, piecewise polynomial approximations of the displacement field generated by a quadrangular FE mesh. In particular, a nine-node Lagrangian element [83,84] is considered (Remark 2). On assuming the continuity of the displacement field at the nodes and along interfaces, the strain is regular, and the NRNT material restrictions on strain have to be enforced inside the elements. Again, the idea is to solve the BVP with a displacement-based method approach through potential energy minimization, taking the effect of settlements as non-homogeneous boundary conditions directly into account.

In this case, the procedure is more complex as the material restrictions are represented by non-linear conditions on the strain that need to be translated in terms of displacements. As shown in Section 1, the latent strain $\mathbf{E}$ has to belong to the positive semidefinite cone:

$$\mathbf{E} \in \mathrm{Sym}^{+}, \tag{25}$$

that, for 2D problems, is equivalent to the two following inequalities:

$$\mathrm{tr}\mathbf{E} \geq 0\ ,\ \ \det\mathbf{E} \geq 0. \tag{26}$$

In the 2D Euclidean space and with respect to a fixed Cartesian reference, the latent strain $\mathbf{E}$ tensor is represented by a 2×2 matrix:

$$\mathbf{E} = \begin{bmatrix} \varepsilon_{11} & \varepsilon_{12} \\ \varepsilon_{21} & \varepsilon_{22} \end{bmatrix}. \tag{27}$$

Analytically, Eq. (25) can be written in terms of Cartesian components, as:

$$\varepsilon_{11}\varepsilon_{22} - {\varepsilon_{12}}^2 \geq 0\ ,\ \ \varepsilon_{11} + \varepsilon_{22} \geq 0 \tag{28}$$

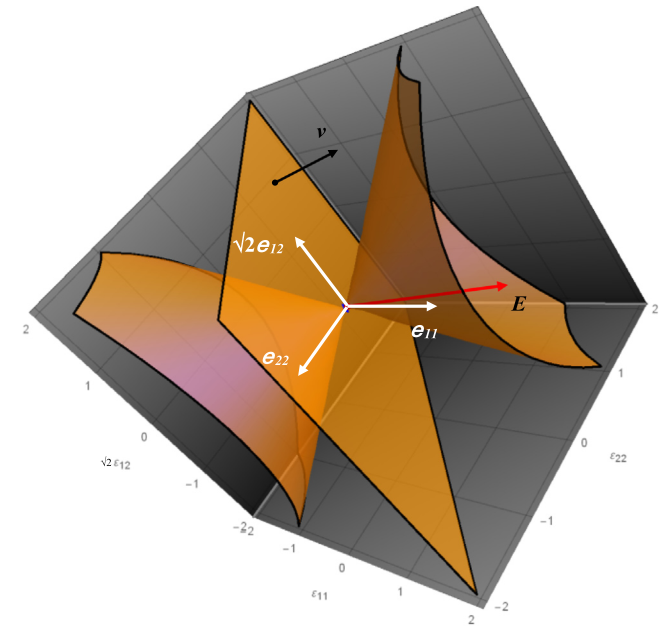

Fig. 4. 3D graphical representation of non-linear condition $\mathbf{E} \in Sym^+$ in the space $\left(\varepsilon_{11}, \varepsilon_{22}, \sqrt{2}\varepsilon_{12}\right)$. The subspace $\mathbf{E} \in Sym^+$ is defined by the intersection of the subset defined by the cone $C : det\mathbf{E} \geq 0$ and the half-space defined by the linear inequality $tr\mathbf{E} \geq 0$. Specifically, the vector $\mathbf{v}$ is orthogonal to the plane $\pi : tr\mathbf{E} = 0$ and points toward the half-space $tr\mathbf{E} \geq 0$. An admissible latent strain $\mathbf{E}$ is represented as a vector.

While relation (28[2]) is linear, condition (28[1]) is non-linear. Nonetheless, once combined together they define a convex set. Indeed, from a geometric standpoint, the condition $\det\mathbf{E} \geq 0$ defines a double cone in the Sym space while the additional condition $\mathrm{tr}\mathbf{E} \geq 0$ selects one of the two cone parts, namely the set of semidefinite positive symmetric tensors, which is also convex (Fig. 4). In Fig. 4 these restrictions are graphically represented referring to the 3D space Sym spanned by the dyadic orthonormal basis $\left(\boldsymbol{e}_1 \otimes \boldsymbol{e}_1\ ,\ \boldsymbol{e}_2 \otimes \boldsymbol{e}_2\ ,\ \sqrt{2}/2(\boldsymbol{e}_1 \otimes \boldsymbol{e}_2 + \boldsymbol{e}_2 \otimes \boldsymbol{e}_1)\right.$.

To keep the optimisation linear, the convex cone (28) is approximated with a finite set of linear relations generated by a number p of tangent planes. To this aim, we first select a set of points equally spaced along a cross-section of the cone; at each point, the corresponding tangent plane is obtained as the plane normal to the local surface gradient. Thus, the set of all tangent planes represents an outer envelope of the cone, as illustrated in Fig. 5. An increasing number of points along the cross section produces a better fit of the conical Sym^+ surface, as depicted in Fig. 5b.

Let Ω be the structural domain discretised with M quadrangular elements, each one associated to a nine-node, Lagrangian element (see Fig. 6). The total number of nodes generated by the adopted shape functions is N. The optimal choice in terms of shape functions, balancing accuracy and simplicity, turned out to be a classical conforming second order 9-node, Lagrangian quadrangular element. In what follows, we refer to this special kind of element and to its shape functions [83]. The partition $(\Omega_{\mathrm{i}})_{\mathrm{i}\in\{1,2,\ldots,\mathrm{M}\}}$ into 9-node rectangular elements, allows to express the displacement field $\mathbf{u}$ as a function of the nodal displacements:

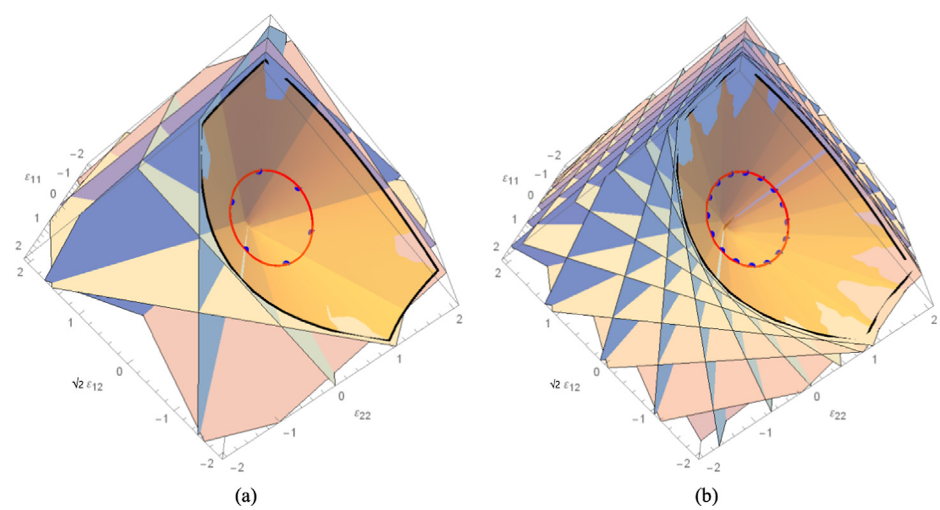

Fig. 5. Two different linearisations of the non-linear material restriction on $\mathbf{E}$ using 6 (a) or 16 (b) tangent planes. The cross-section of the cone obtained using a plane orthogonal to the cone-axis is a circumference where p equally spaced points are selected to "generate" the linear outer envelope.

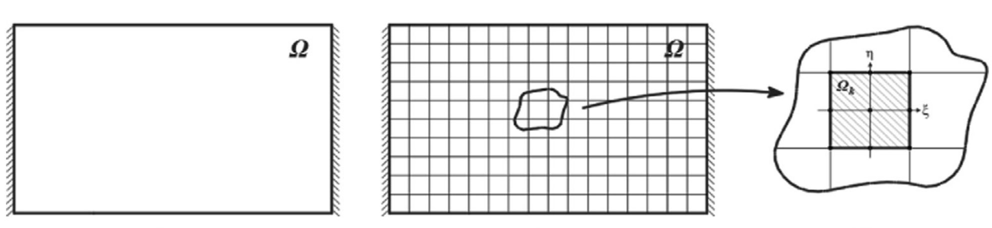

Fig. 6. The infinite-dimensional space $\mathscr{K}_c$ of continuous displacements with support in Ω (a) is discretized considering a partition $(\Omega_i)_{i\in\{1,2,\ldots,M\}}$ of the whole domain into e.g. quadrangular elements (b): the finite dimensional approximation generated by the fixed partition is called $\mathscr{K}_c^N$, where N is the number of nodes. In (c) a subdomain Ω_k and a second order Lagrangian element with 9-node is depicted.

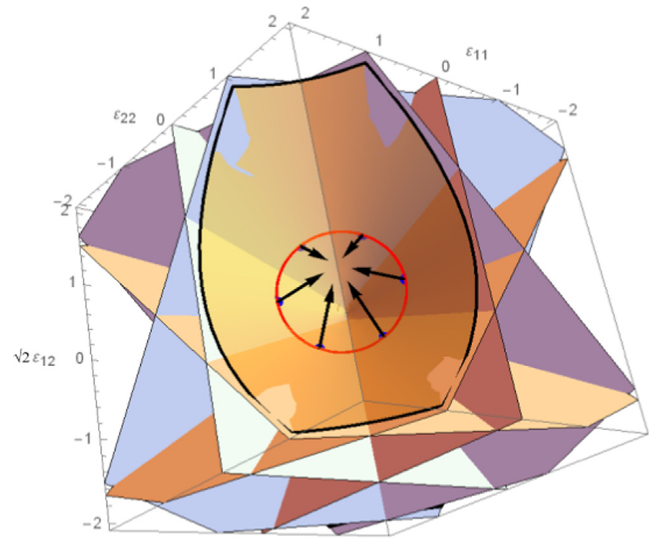

Fig. 7. Envelope of the cone with 6 tangent planes and surface gradient vectors at the generating points. The condition $\mathbf{E}_k\left(\tilde{x},\tilde{y}\right) \in Sym^+$ is discretized by using the gradient vectors to construct the system of inequalities $\mathbf{A}_k\left(\tilde{x},\tilde{y}\right)\hat{\boldsymbol{U}}_k \geq 0$.

$$\mathbf{u} = \mathbf{u}(\mathbf{U}), \tag{29}$$

with $\mathbf{U} = (U_1, V_1, .., U_i, V_i, .., U_N, V_N)$ and in which (U_i, V_i) denotes the displacement of the node i. With this discretisation, the minimum problem (10) can be approximated through the following finite dimensional one:

$$\wp(\mathbf{u}^o_{CDF}) = \min_{\mathbf{u}\in\mathscr{K}^N_C} \wp(\mathbf{u}), \tag{30}$$

where $\mathscr{K}^N_C$ denotes the discretised set of kinematically admissible displacement generated by the given FE mesh partition of the structural domain.

The displacement field in any finite element Ω_k can be expressed as a function of the nodal displacement (U_j, V_j) as

$$\mathbf{u}_k = \mathbf{u}|_{\Omega_k} = \boldsymbol{f}(U_j, V_j), \tag{31}$$

where $\boldsymbol{f}$ accounts for the adopted Lagrangian shape functions. The latent strain can thus be expressed as function of the nodal displacements:

$$\mathbf{E}_k = \mathbf{E}|_{\Omega_k} = \mathrm{Sym}\nabla\mathbf{u}_k. \tag{32}$$

The material restriction (25) are enforced at each Gauss node whose coordinates are $\left(\tilde{x},\tilde{y}\right)$ (see Fig. 7), as:

$$\mathbf{E}_k\left(\tilde{x},\tilde{y}\right) \in Sym^+. \tag{33}$$

Using the above-described linearisation scheme, conditions (33) can be approximated with the following set of p inequalities:

$$\mathbf{A}_k\left(\tilde{x},\tilde{y}\right)\mathbf{U}_k \geq 0, \tag{34}$$

with $\mathbf{A}_k\left(\tilde{x},\tilde{y}\right)$ a matrix of p rows and $\mathbf{U}_k$ the vector collecting the nodal displacements of the element k. Note that, combining (31) and (32), the condition (33) is expressed in terms of nodal displacements (34).

Inequalities (34) have to be written for all Gauss points of the mesh. Once all these relations are collected, the material restriction (24) can be expressed on the whole domain as:

$$\mathbf{AU} \geq \mathbf{0}. \tag{35}$$

The non-homogeneous boundary conditions can be easily expressed as:

$$\mathbf{BU} = \mathbf{U}_s. \tag{36}$$

where $\mathbf{B}$ is the extractor operator that selects the nodes on the constrained boundary, while $\mathbf{U}_s$ collects the prescribed displacements. Inequalities (54) together with boundary conditions (55) define the set of admissible displacements:

$$\mathbb{K}^N_{CDF} = \left\{\mathbf{U} \in \mathbb{R}^{2N} \ / \ \mathbf{AU} \geq 0 \ , \ \mathbf{BU} = \bar{\mathbf{U}}\right\} \tag{37}$$

that represents the admissibility domain of the optimisation problem, whose objective function is represented by the total potential energy. Therefore, the minimum problem (10) can be discretised as:

$$\wp(\mathbf{U}^o_{CDF}) = \min_{\hat{\mathbf{U}}\in\mathbb{K}^N_{CDF}} \wp(\mathbf{U}). \tag{38}$$

With the above approximation the structural problem is reduced to the following minimum problem: "*Find a nodal displacement vector $\mathbf{U}^o_{CDF}$ which minimizes the potential energy $\wp$ in $\mathbb{K}^N_{CDF}$*". This minimum problem is still a linear programming problem since the energy is linear and the material restrictions are reduced to be linear inequalities. In the present case, once the minimiser $\mathbf{U}^o_{CDF}$ has been obtained it is possible to construct the deformed shape of the structure, and, as we will show, the best way to graphically show the fracture field is to plot the corresponding rotation and strain fields.

Remark 2. *We must say that the type of element that can be considered to approximate the displacement field is not completely free. Indeed, linear or bilinear elements cannot properly work because of their inability in reproducing simple uniaxial flexure, a mechanism that is often required to simulate non-uniform cracks (i.e. cracks due to relative rotation along a straight line).* ■

Remark 3. *In real masonry structures, the appearance of piecewise rigid mechanisms (associated to concentrated fractures) rather than continuous mechanisms (entailing diffuse fractures), is often due, to mechanical characteristics (e.g. cohesion, toughness and finite friction) also depending on construction techniques. This mechanical aspects are not taken into account by the NRNT model. Indeed, for NRNT materials, it is in general not possible to prefer concentrated cracks over diffuse fractures. This circumstance is essentially due to the absence of any energy-growth property on unbounded fracture strains. An energy-growth property for displacement fields in* BD(Ω) *is restored by introducing the so-called Safe Load Condition as proved in* [72,73]. *The safe load condition consists of adding an isotropic pressure all over the loaded boundary. Without such confinement, the energy is not coercive, meaning that the displacement can grow indefinitely at zero energy price. In our model, this confinement is imposed by adding, all over the loaded boundary, an artificial given uniform pressure of very small magnitude, that is of the order of* 10^{-2} *to* 10^{-3} *of the mean compressive stress* σ_m. *The presence of such a negligible (with respect to the given loads) value of isotropic pressure, also has the effect of encouraging rigid block mechanisms over diffuse deformations. This trick is sufficient to provide the BVP with the Safe Load Condition, to avoid zero-energy modes and to make rigid block deformations/ concentrated cracks the preferred minimum-energy mechanism.*■

4. Applications

In this section, we consider some specific problems of increasing complexity to illustrate the CDF method and to compare its results with the PRD method. The CDF numerical problem is implemented in Wolfram Mathematica® [85]. The solution of the linear programming problem is then obtained through specific Python scripts by means of CPLEX Optimisation Software [86]. Conversely, the PRD analyses are performed through *compas_prd* [70]. All analyses were performed with an Intel® Core™ i7-8850HQ. In all CDF analyses, if not differently mentioned, we enforce the Safe Load Condition (Remark 3) by considering a uniform isotropic pressure equal to 10^{-3} of the mean compressive stress (Section 4.4.1). Lastly, in all CDF analyses, the convex cone is approximated using 64 planes.

4.1. Lintel subjected to horizontal outward displacement

As first case, we look at a trivial but emblematic problem: the lintel (plat-band) under vertical loads (Fig. 8a). The lintel of Fig. 8a, supposed to be made of Heyman's material (i.e. to be no-tension but with infinite compressive strength), can resist to infinite vertical loads. In reality, it thrusts horizontally, and this thrust could make the abutments give way a little. Thus, the lintel accommodates its increased span by developing three fractures. These cracks define two rigid macroblocks (Fig. 8b) hinged at three points and forming a statically determined structure: a three-pinned arch. To reproduce this behaviour with both the PRD and the CDF methods, we formulate the BVP for this body made of NRNT material, uniformly loaded at the top edge, and subject to constraints at the two lateral edges which spread horizontally by a given amount δ, as shown in Fig. 8a.

4.1.1. Analytical solution

In Fig. 8b, an analytical solution of the BVP of Fig. 8a, obtained by admitting singular stress and strain fields, is presented. The structural domain, considered as closed along the constrained boundary, shows three concentrated strain fractures. The red cross-hatching denotes the singular deformations $\mathbf{E}^s$ along the three fracture-lines. The blue, dash-dotted line represents the support of a singular stress field $\mathbf{T}^s$ in equilibrium with the given loads: this could be thought of as a 1D arch supporting the load with a singular stress. The regular part of the stress is a vertical compressive uniaxial stress field located above the arched line (transferring the load from the upper boundary to the thrust line) and a zero-stress below it. The uniaxial stress field is discontinuous across the line of thrust and is balanced by a concentrated singular stress having the curved line (a parabola) as its support. Both the displacement and the stress fulfil the corresponding material restrictions (1^1) and (1^2). Furthermore, the fields depicted in Fig. 8b satisfy the material restrictions (1^3), that is $\mathbf{T}\cdot\mathbf{E}=0$. Therefore, these stress and strain fields represent a possible solution of the BVP.

4.1.2. PRD analysis

In this section, we apply the PRD approach to solve the BVP of Fig. 8a. As reported in Fig. 9a, the panel is discretised into 160 rigid, square elements. The uniform distributed load, represented with a rectangular yellow strip, is the only force contribution to the total potential energy. The two constrained left and right edges are subjected to a given outward settlement δ.

The non-homogeneous boundary conditions, expressing the outward settlements, can be written in terms of the displacements of the nodes lying on the constrained boundary. In particular, for each of such nodes P one can write:

$$\mathbf{u}(\mathrm{P})\cdot\mathbf{t}=0, \tag{39}$$

$$\mathbf{u}(\mathrm{P})\cdot\mathbf{n}\leq\delta. \tag{40}$$

Specular relations have to be written for the left side. These boundary relations combined with the internal ones, define the subset $\mathbb{K}^{M}_{PRD}$ (in which the optimal solution has to be found. The total number of unknowns (i.e. the dimension of $\widehat{\mathbf{U}}$) is 540. The number of internal equality and inequality conditions, defining the subset $\mathbb{K}^{M}_{PRD}\subseteq\mathscr{R}^{540}$, is 1920. The solution $\mathbf{U}^{o}_{PRD}$ of the minimum problem (23) is reached through the simplex method and the computational time is about 0.03 s. A graphical representation of $\mathbf{U}^{o}_{PRD}$ is reported in Fig. 9b. It can be observed that three hinges form and the panel, initially a statically overdetermined structure with many redundancies, transforms into an isostatic structure made of two blocks and articulated through three hinges. The PRD solution exactly coincides with the analytical solution reported in Fig. 8b.

4.1.3. CDF analysis

Here, the same problem is analysed using the CDF method. Two different discretisations, as shown in Fig. 10, are considered to illustrate the possible dependence of CDF on the mesh. With the first one, we want to look for the solution by using an even number of elements along the horizontal axis (Fig. 10a). Conversely, with the second we seek the solution utilising a discretisation with an odd number of elements (Fig. 10b). As we said above, we adopt second-order Lagrangian elements: 60, nine-node square elements in the first case, and 66, 9-nodes, rectangular elements in the other case. The only load considered is again a uniformly distributed vertical load acting along the top edge. The supports are supposed to

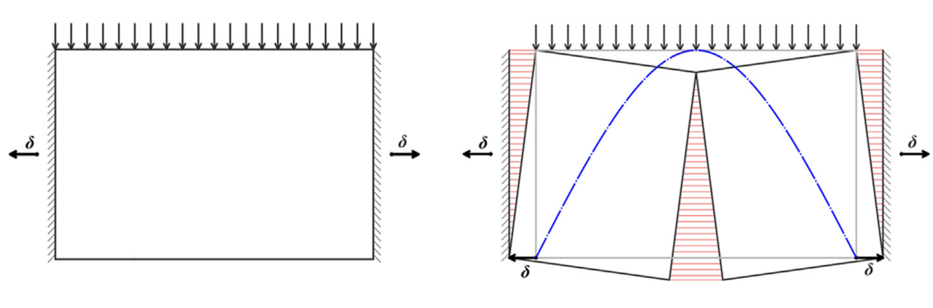

Fig. 8. In (a): panel of NRNT material subjected to a uniform load applied along the top edge and to symmetric, outward, horizontal settlements. In (b): possible solution of the BVP of Fig. 8a obtained by using singular stress and strain fields. The red cross-hatching represents the singular deformations $\mathbf{E}^s$ along the three fracture lines; the dash-dotted line represents the support of a singular stress field $\mathbf{T}^s$ in equilibrium with the given loads. These two admissible fields satisfy the condition $\mathbf{T}\cdot\mathbf{E}=0$ and, thus, represent a possible solution of the BPV. (For interpretation of the references to colour in this figure legend, the reader is referred to the web version of this article.)

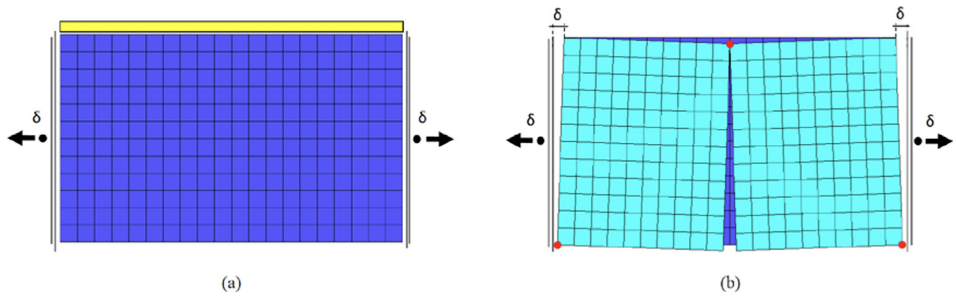

Fig. 9. In (a): a NRNT lintel loaded on the top edge by a uniformly distributed load (yellow strip) and subjected, along the left and right edges, to given outward settlements, is discretized into 160 square elements. In (b): graphical representation of the PRD solution $\mathbf{U}^{o}_{PRD}$ of the minimum-energy problem (23): the panel becomes an isostatic three-pinned arch (pins depicted with red dots). (For interpretation of the references to colour in this figure legend, the reader is referred to the web version of this article.)

spread outward as depicted in Fig. 10 and the non-homogeneous boundary conditions are enforced through Eqs. (39) and (40).

The solution $\mathbf{U}^{o}_{CDF}$ of the minimum problem (38), reported in Fig. 11**,** is reached in both cases using the interior-point method in about 1.20 s. Particularly, Fig. 11a [Fig. 11b] shows the results obtained using the discretisation of Fig. 10a [Fig. 10b]. In the second row of Fig. 11, we report the contour plot of $|\mathbf{E}| = \mathrm{tr}\left(\mathbf{E}\mathbf{E}^{T}\right)^{1/2}$ as a measure of the intensity of the strain field. Both analyses disclose large deformation gradients concentrated on a central strip. In Fig. 11c, large strain gradients affect both the two vertical stripes located on both sides of the middle line. Conversely, with the second discretisation, the gradient of the latent strain concentrates over the central elements only (Fig. 11d). In both analyses, most of the structural domain exhibits zero-strain, meaning that these parts are moving quasi-rigidly. In the third row of Fig. 11, the contour plot of the skew-symmetric part of the displacement field (i.e. the local rotation field) is reported. The rotation is exactly symmetric and almost piecewise uniform. The uniformity of the rotation field over most of the domain is a further indication of the smallness of the pure deformation.

4.1.4. Discussion

In the present section, we discuss and compare the approximate solutions obtained with both methods. The PRD analysis returns three fractures, and the initially overdetermined lintel becomes a statically determined three-pinned arch (Fig. 9b). This mechanical behaviour can be seen from the CDF results also. Indeed, as already noted before, most part of the structure is behaving as rigid, and both the gradient of strain and rotation fields are concentrated along a middle vertical line. To highlight this behaviour and compare the two methods, in Fig. 12 we report some additional graphical results extracted by the two different CDF analyses. The first row of Fig. 12 shows two diagrams of the stream plot of the displacement field exhibited by the lintel as obtained with CDF by using the two different meshes. The two-stream plots are very similar and, as one expects, indicate a three-pinned arch mechanism, which, in both cases, is pivoting about the two symmetric corner points (0, 3) and (5, 3).

Moreover, in the second row of Fig. 12, the area where the strain is non-zero (namely greater than 10^{-4} of the mean strain) is depicted in white. This further indicates that the structure nucleates essentially into two rigid bodies. In particular, this aspect is also and more clearly highlighted in the last row of Fig. 12 where positive rotations are depicted in red and negative ones in blue: a neat subdivision of the domain into two blocks can be seen. Finally, from the CDF method, we obtain essentially the same results of the PRD analysis: the structure becomes a three-pinned arch as two clear sub- macro-regions form and displace essentially as rigid bodies. Indeed, these two rigid sub-regions show approximately constant rotation coupled with a negligible deformation.

4.2. The case of a slanted crack

Mesh dependency is a given fact for FE with strong discontinuities [84]. A typical way out is to use remeshing. In the present section, we propose a benchmark case to test the efficiency of the PRD and CDF method with regard to this issue. We consider the case of a panel of NRNT material, loaded and constrained as shown in Fig. 13a. This is another non-homogeneous *mixed problem*, since part of the boundary is loaded and the remaining constrained part is displaced. Indeed a portion of the bottom constraint is subjected to a given linear settlement as in Fig. 13a. A diagonal crack of the form labelled with the bold slanted (Fig. 13c) is expected.

4.2.1. Analytical solution

Using singular strain and stress fields, a possible analytical solution of the mixed BVP (Fig. 13a) is represented in Fig. 13b, c. Indeed, the stress field depicted in Fig. 13b is statically admissible, the displacement field represented in Fig. 13c is kinematically

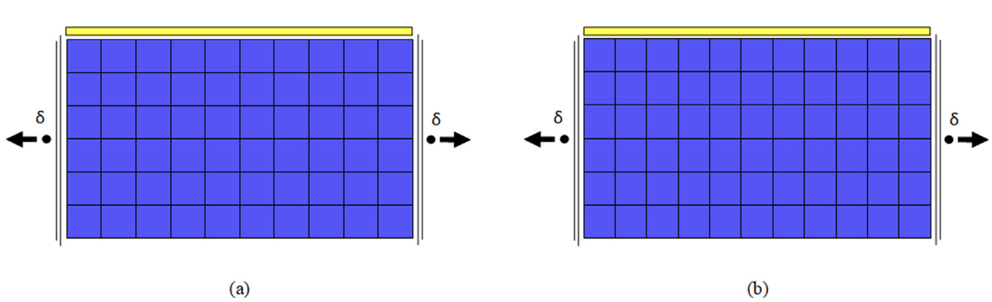

Fig. 10. Two different discretisations of the NRNT panel of Fig. 8a. In (a) the domain is divided into 60 nine-node square elements while in (b) 66 elements are considered. The only load consists in a uniformly, distributed, vertical load applied at the top edge and is represents the only work term of the total potential energy. The left and right side are subjected to given outward displacements.

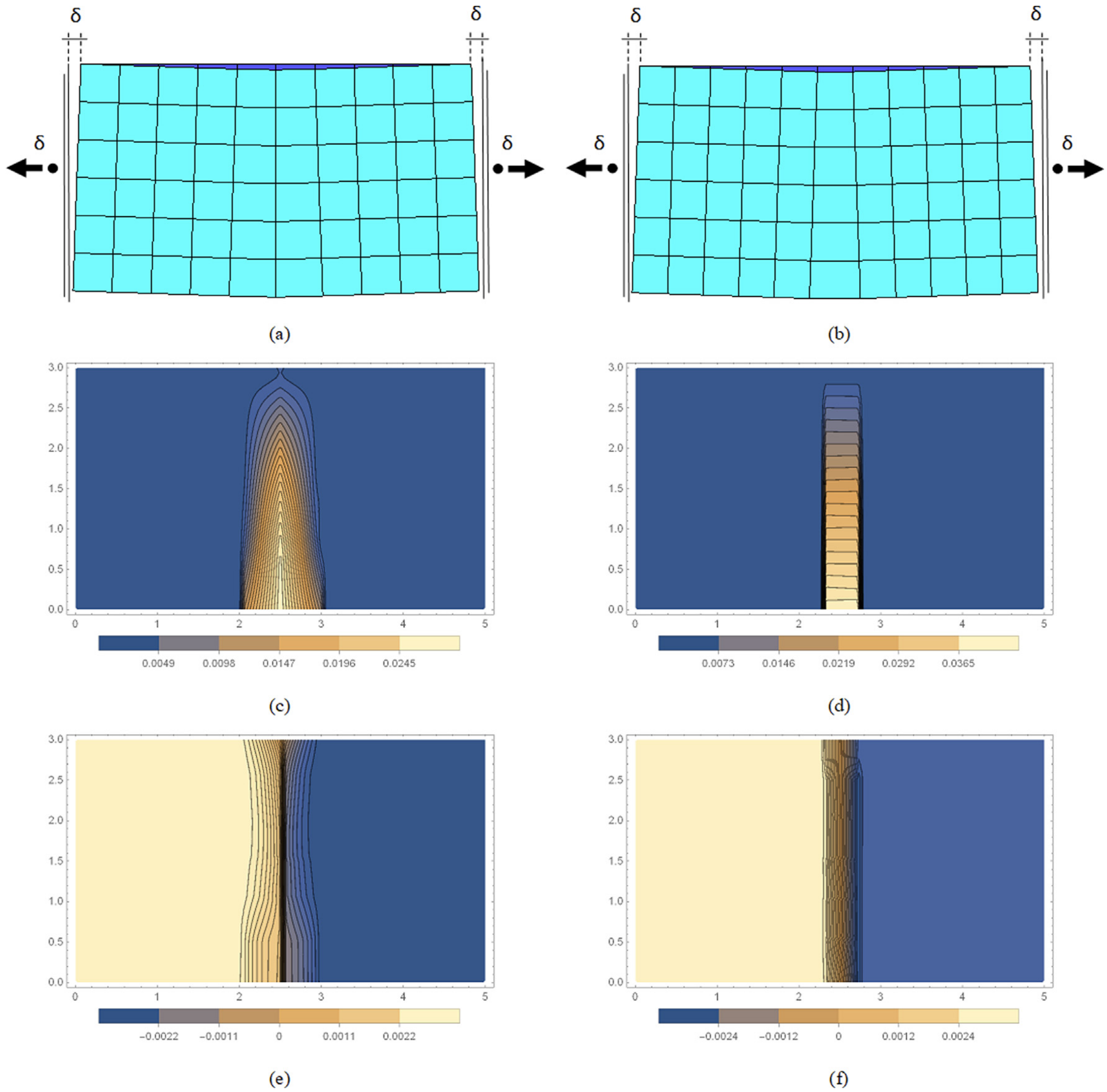

Fig. 11. Graphical representation of the solution $\mathbf{U}^{o}_{CDF}$ of the minimum problem (38) for both the discretisations adopted: (a, b). In (c, d): contour plots of $\sqrt{\mathrm{tr}\left(\mathbf{E}\mathbf{E}^{T}\right)}$. In (e, f): contour plots of the rotation fields.

admissible, and they satisfy the condition $\mathbf{T}\cdot\mathbf{E}=0$, i.e. Eq. ($1^3$). In this sense, they represent a possible solution of the mixed BVP of Fig. 13a.

4.2.2. PRD analysis

In this section, we apply the PRD method to solve the BVP of Fig. 13a, assuming three different discretisations as in Fig. 14 to illustrate how the solutions provided by the PRD approach can approximate the analytical one depicted in Fig. 13c. The first discretisation (*case1*) is composed of 160 rigid, square blocks (Fig. 14a); the second one (*case2*) is obtained partitioning each rigid square block into 4 triangles, so it counts 480 triangle, rigid elements (Fig. 14b); finally, the third discretisation (*case3*) is defined using 1440 triangles to match the potential diagonal crack we expect (Fig. 14c), that is the element interfaces run along the expected fracture line. In all cases, the uniform distributed load is represented by rectangular strips and part of the boundary is fixed whilst part of the bottom edge is subjected to a given linear settlement, as specified in Fig. 14.

The PRD solution of *case1* returns a vertical crack, and is unable to reproduce, even approximatively, the expected crack. The numerical solution associated to *case2* returns the crack pattern shown in Fig. 14e. As one can see, the numerical solution approximates the expected diagonal crack better. The exact solution is reached when the PRD method is applied to *case 3*: it returns the analytical one exactly. Moreover, depicting the rotation field using different colours to map positive and negative rotations, it is possible to see how refining the original square-element discretisation, the diagonal crack is increasingly approximated even if in a weak sense. Indeed, looking at Fig. 14h, even if the discretisation is not the most appropriate, the solution tends to match the diagonal crack from a certain point onwards.

4.2.3. CDF analysis

In the present section, to illustrate the influence of the mesh size, we propose the CDF analysis of the NRNT panel described in Fig. 13a using two different discretisations: the first is composed of 60 square, 9-node, Lagrangian elements (Fig. 15a), while the second one discretises the panel into 240 square, 9-node, Lagrangian

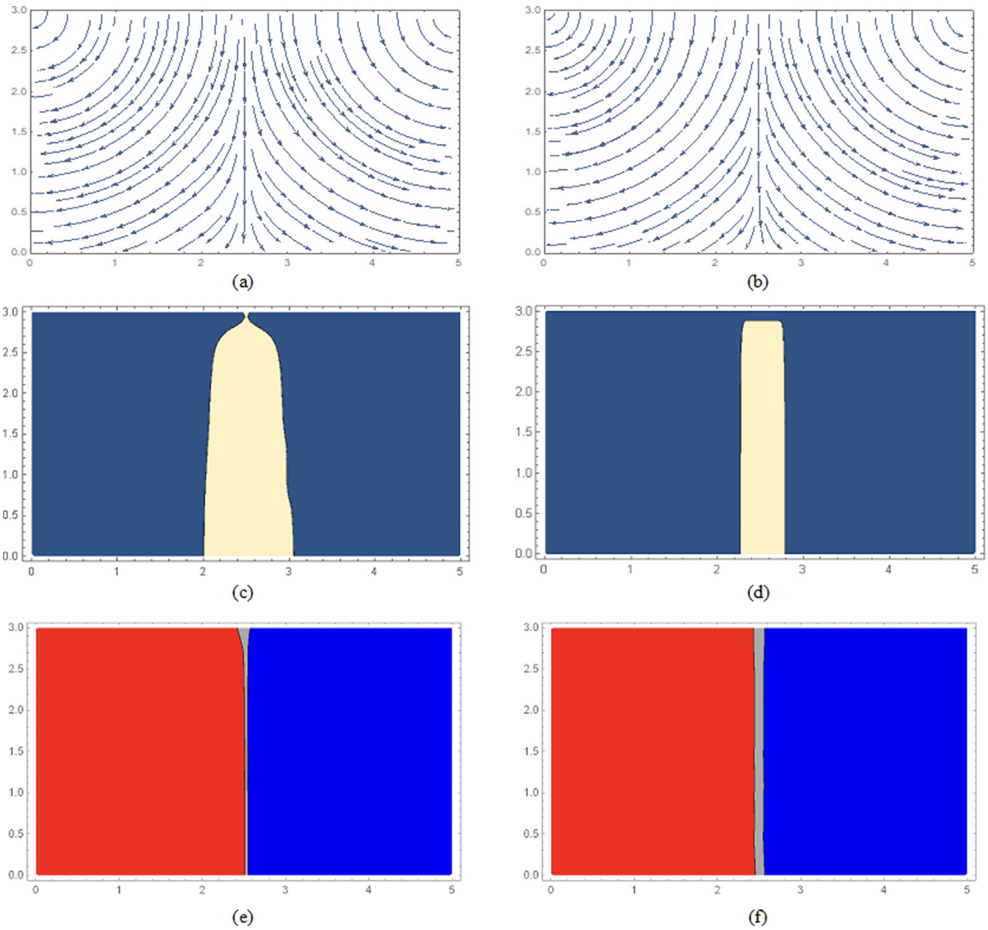

Fig. 12. In (a, b): stream plots of the displacement field solving the CDF problems. In (c, d): the regions over which the deformation is essentially zero are depicted in blue, while, the white denotes the areas of non-zero strains. Finally, in (e, f) the positive rotations are in blue while the negative ones are depicted in red. In both CDF analyses, the structural domain nucleates into two rigid macroblocks behaving as a three-pinned arch. (For interpretation of the references to colour in this figure legend, the reader is referred to the web version of this article.)

elements (Fig. 15b). The uniform load is applied along the top, loaded part of the boundary.

The CDF solutions $\mathbf{U}^{o}_{\mathrm{CDF}}$ of these minimum problems are obtained through the interior point method in 0.91 s (Fig. 15a) and 17.30 s (Fig. 15b), respectively. The corresponding displacements are depicted in Fig. 16a-b. Looking at the displacements, in both cases, it can be easily seen that the point {2.0, 0.0} represents the centre of rotation for the moving part of the panel. In Fig. 16c-d, to represent the strain field $\mathbf{E}$, we report the graph of a measure of the deformation, namely the contour plot of $|\mathbf{E}|^2 = tr\left(\mathbf{E}\mathbf{E}^{\mathrm{T}}\right)$: the gradient of deformation is concentrated along a narrow band located in the vicinity of a slanted line, whilst the other elements are characterized by strains whose norm is close to zero. The skew-symmetric part of the displacement field, representing the local rotation field, is depicted in Fig. 16e-f. It should be noticed that the gradient of rotation is also essentially concentrated along a slanted line. These results are even more highlighted if one looks at the results shown in Fig. 17, where the first row shows the non-zero strain areas and, more importantly, the second rows illustrates the trend of positive and negative rotations over the whole domain. Particularly, Fig. 17c-d shows a clear subdivision of the structural domain into two parts, whose boundary identifies a slanted crack approaching exactly the rotation point {2.0, 0.0}. Furthermore, looking at the non-zero strain regions (Fig. 17-a-b), a finer discretisation tends to narrow down the non-zero strain are, and consequently, to better approximate the expected slanted crack.

4.2.4. Discussion

The previous problem exemplifies the main shortcoming of the PRD method: the solution is unable to converge to a concentrated crack whose support is not parallel to the skeleton of the mesh. Nonetheless, by refining the mesh, the solution shows a weak convergence to the exact one. The inability to catch a diagonal crack inherent to the PRD method, can be explained as follows. Let us consider the problem of Fig. 13a and the coarse mesh of Fig. 18a.

A rigid block mechanism approximating a diagonal crack is shown in Fig. 18b. Such an approximation of the diagonal crack produces non-zero relative sliding among elements lying along the zig-zag fracture line. Heyman's model forbids sliding of two adjacent elements, one upon another; then this piecewise rigid displacement field, is not kinematically admissible. Therefore, we cannot use zig-zag cracks to approximate slanted cracks. Different strategies can be adopted to overcome this issue [87], and one of them could come from a comparison with the CDF solution. As the CDF method does not suffer from mesh dependency, it can be used either as an alternative of the PRD method to model complex structures or, in combination with it, as a useful remeshing strategy to inform the PRD discretisation.

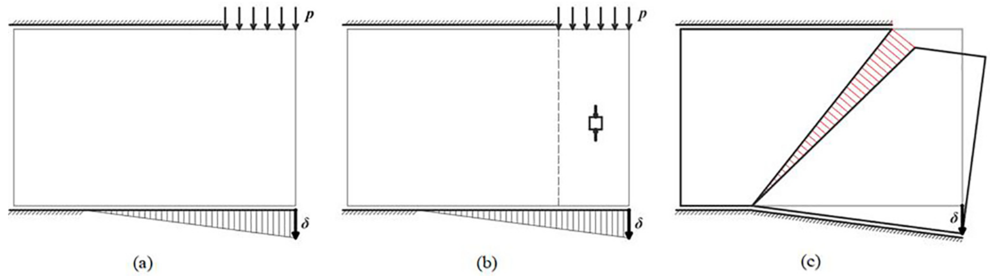

Fig. 13. Mixed BVP for a panel of NRNT material subjected to a given linear settlement (a). In (b,c): possible analytical solution of the BVP depicted in Fig. 13a, using a regular stress field $\mathbf{T}^r$ (b) and a singular strain field $\mathbf{E}^s$ (c) such that $\mathbf{T}^r \cdot \mathbf{E}^s = 0$. The expected diagonal crack (c) is the support of the singular deformation $\mathbf{E}^s$ labelled with the red-crosshatch.

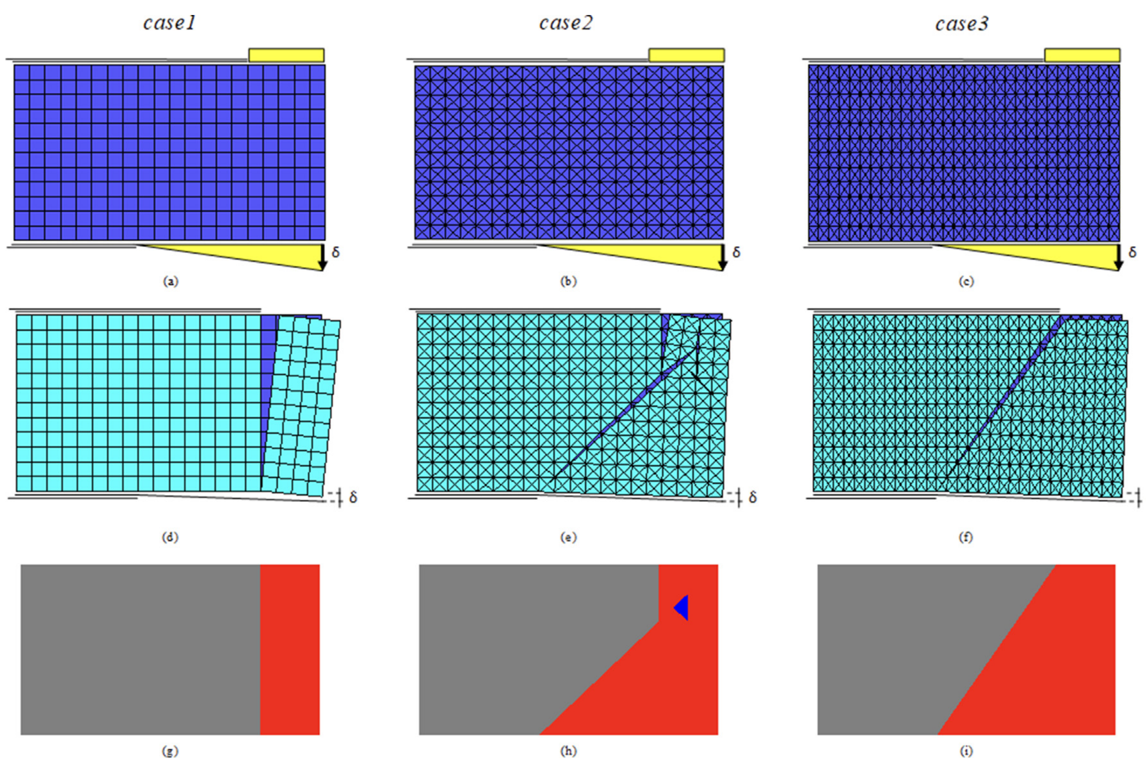

Fig. 14. PRD analysis of the NRNT panel of Fig. 13 using three different discretisations. Refining the original square-element discretisation, the diagonal crack is increasingly approximated.

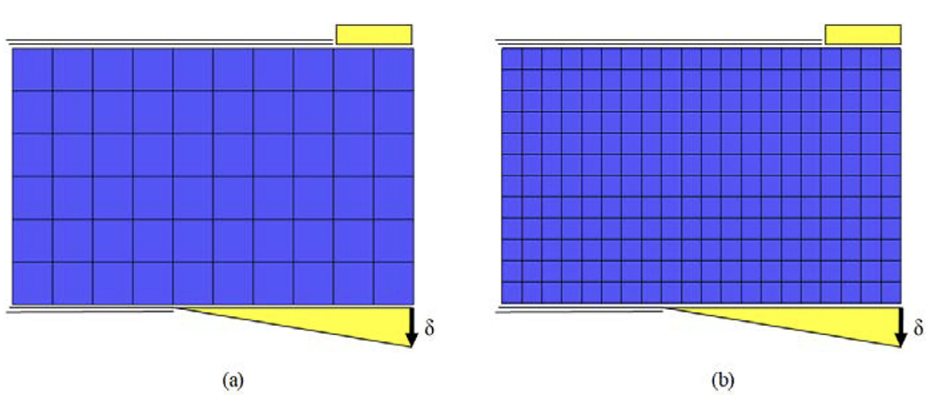

Fig. 15. The NRNT panel of Fig. 13 is discretised using two different meshes based on 9-node, Lagrangian elements: the first one looks for the solution of the mixed BVP with 60 squares (a), while the second one uses 240 squares (b).

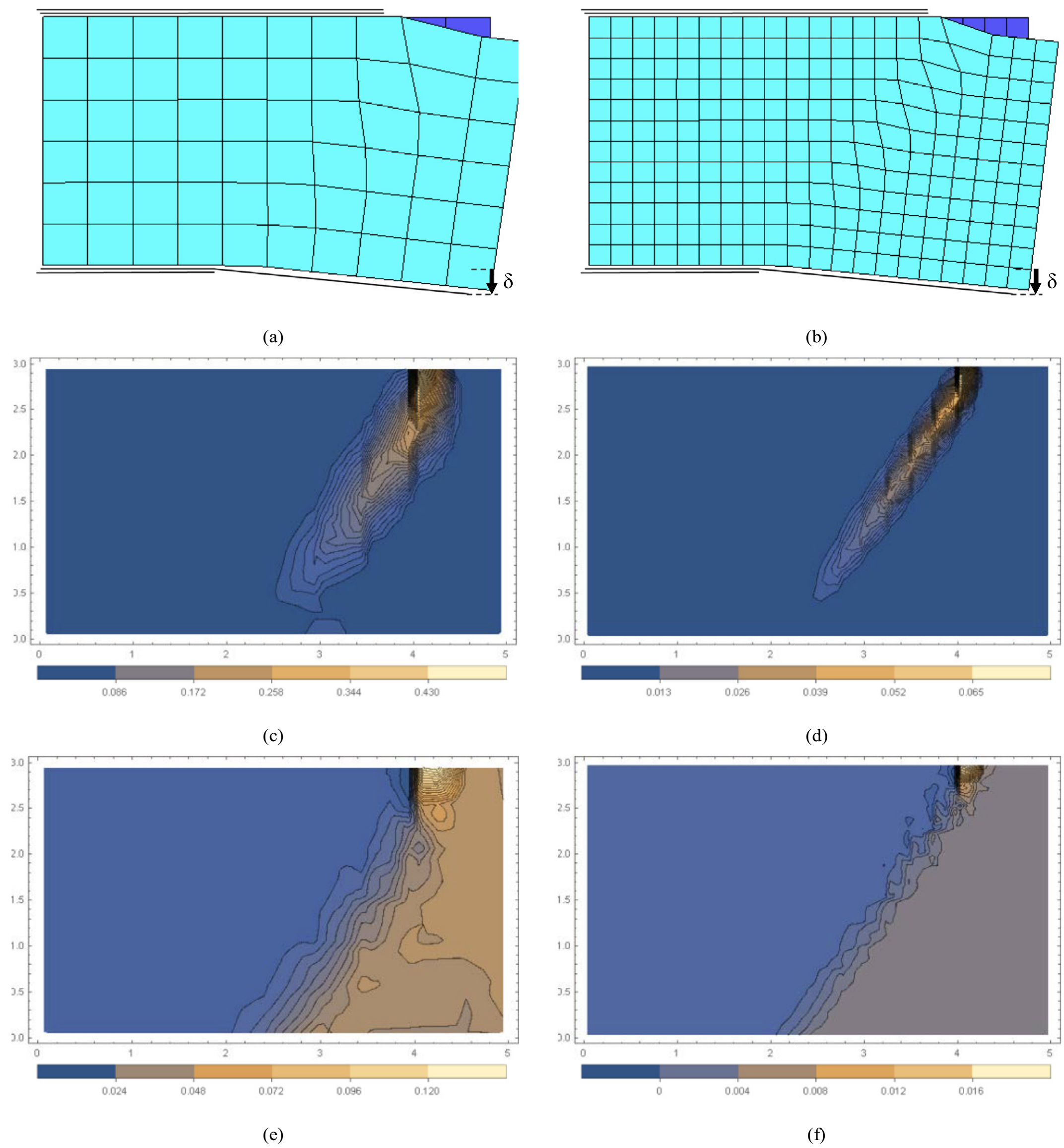

Fig. 16. CDF solutions of the panels shown in (Fig. 15). The first row shows the solution in terms of displacement fields (a, b). The second and third rows illustrate the measure of the strain tensor as $|\mathbf{E}|^2 = tr\left(\mathbf{E}\mathbf{E}^{\mathrm{T}}\right)$ (c, d) and the rotation field (e, f) over the whole domain, respectively.

Remark 4. *If we look at the picture in* Fig. 18a *as an image of a real structure made of square blocks, the deformation of* Fig. 18b *represents a reasonable outcome of the given settlement. Nonetheless, such a mechanism can be thought of as a non-Heymanian mechanism as defined by Bagi in* [88]*. Of course no real wall, even made of dry stones without mortar, is constructed without any kind of interlocking, therefore the deformation we see there, is actually not realistic. The NRNT model represents a sort of qualitative homogenization of the behaviour of masonry structures made of well-constructed masonry elements. The assumption of no sliding, based on the way masonry is constructed and interlocked, is essential for our minimum energy scheme to work, and the reason of the discrepancy between what we see in* Fig. 16b *and the predictions of our model resides in the size of the representative volume element for our "homogenized" continuum, which must be large compared to the size of the individual "real" blocks. We must say that, when the structure is made of large blocks one should admit sliding among blocks at some degree. This can be done, preserving the minimum energy principles and the theorems of Limit Analysis, by considering non-homogeneous interface conditions (that is conditions of the type* (12) (13) *with a known term). The meaning of this known term is to allow some clearance among blocks, that is, a possible relative displacement in the "forbidden" direction of a limited value. As long as these relative displacements are limited the theorems of limit analysis and the minimum principles remain valid.*

4.3. A simple masonry portal undergoing a vertical settlement

In this section, we illustrate the case of a simple NRNT-portal, loaded on the top edge by a piecewise uniformly distributed load p and subjected to a given vertical settlement of the right support (Fig. 19a).

4.3.1. Analytical solution

Using singular strain and stress fields, an analytical solution of the mixed BVP of Fig. 19a, can be constructed partitioning the structure into three rigid pieces, as depicted in Fig. 19b. Looking at this three-block discretisation, the displacement due to the vertical settlement is represented by a three-hinge mechanism, and depends univocally on the variable x defining the position of the

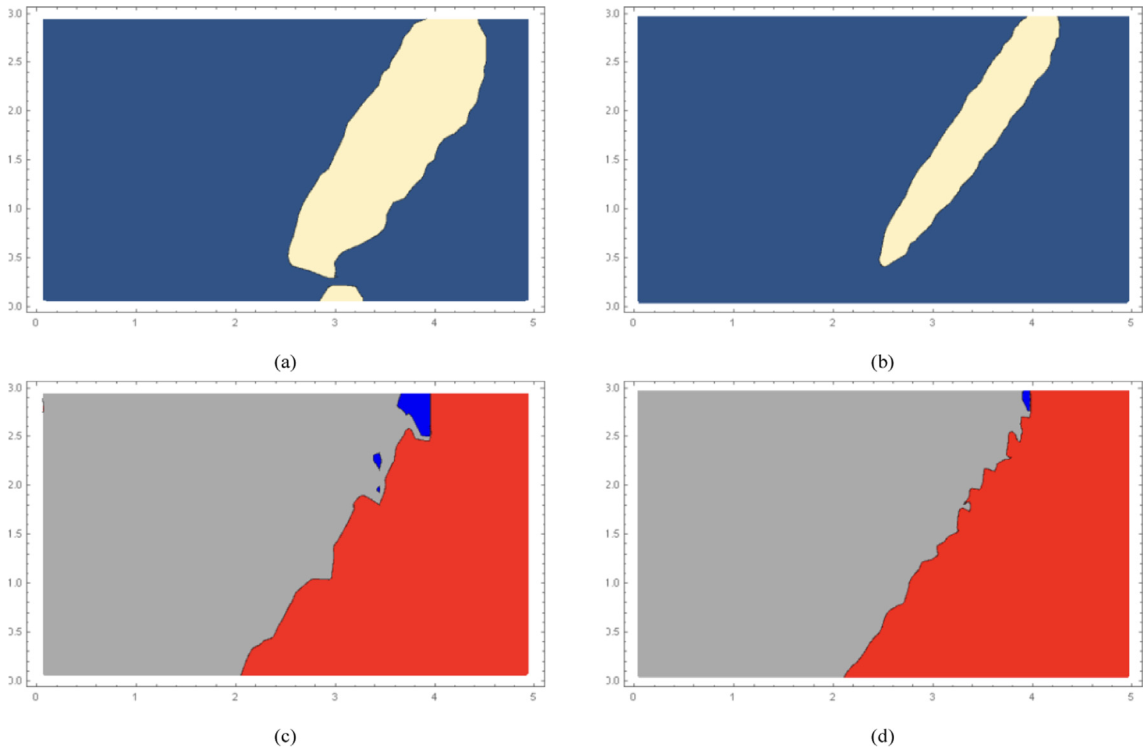

Fig. 17. In (a, b): the white-regions identify the area where the strain is non-zero (i.e. $|\mathbf{E}|^2 = tr\left(\mathbf{E}\mathbf{E}^{\mathrm{T}}\right)$. In (c, d): positive and negative rotation are labelled in red and blue, respectively. (c, d) shows a clear subdivision of the structural domain into two macroblocks behaving as rigid as the strain is almost constant over them. (For interpretation of the references to colour in this figure legend, the reader is referred to the web version of this article.)

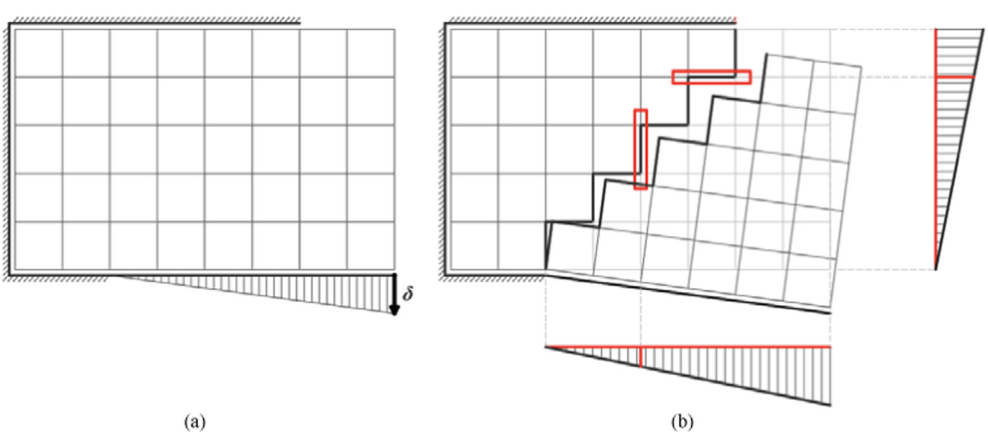

Fig. 18. The NRNT panel of Fig. 13a discretized into 40 square elements (a). The approximation of a diagonal crack using square elements and the profiles of the horizontal and vertical displacements of the moving block are reported (b). From them we see that any two adjacent blocks lying along the opening exhibit relative sliding (as shown graphically for the two highlighted interface segments).

central hinge (Fig. 19a). The corresponding strain field is purely singular and fulfils Eq. (1^2). Specifically, the exact position x is obtained by analytically minimizing the total potential energy:

$$x = \frac{-a(b+l)^2 + \sqrt{a(b+l)^2\left(a(b+l)^2 + h\left(2bl + l^2 + b^2\gamma\right)\right)}}{h(b+l)} \tag{41}$$

with $\gamma = p_2/p_1$. Looking at the geometry shown in Fig. 19, characterized by b = 1.75 m, l = 2.50 m, h = 3.00 m and a = 2.00 m, and assuming $\gamma = 1$, the exact position of the central hinge is $x/l = 0.658$.

A statically admissible stress field satisfying Eq. (1^1) consists of a vertical uniaxial stress emanating from the top load and a singular stress concentrated on the curved line passing through the three hinges as in Fig. 19b. Particularly, the support of the singular stress field, being the curve tangent to the upper boundary of the lintel (i.e., at the central hinge), is entirely contained within the structural domain: in this sense it represents a pure compressive admissible stress field. The strain and stress fields, as constructed, satisfy the compatibility relation Eq. (1^3), that is, they represent a possible analytical solution of the BVP.

In what follows, to illustrate the dependency on the mesh size and the convergence of both approaches, we show the results obtained with both numerical methods using two different meshes. Specifically, the NRNT portal of Fig. 19a is discretised using 360 and 1140 square elements, respectively (Fig. 20). The NRNT portal is subjected to a uniformly distributed load (rectangular, yellow strip), and the right support is subjected to a given, uni-

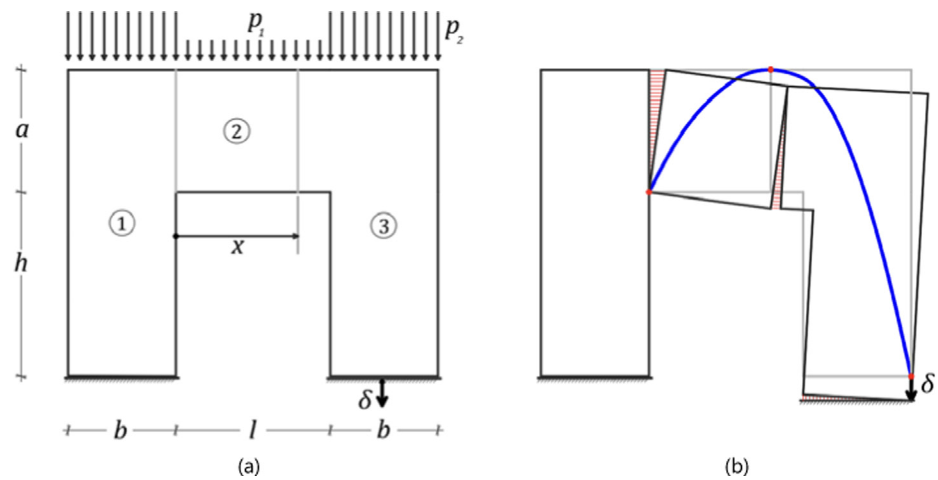

Fig. 19. Mixed BVP for a simple portal of NRNT material loaded along the top surface and subjected to a given vertical settlement (a). An analytical solution of the BVP depicted in Fig. 19a, considering a regular and singular stress field $\boldsymbol{T}$ and a purely singular strain field $\boldsymbol{E}^s$ such that $\boldsymbol{T} \cdot \boldsymbol{E} = 0$, is reported in (b). Three hinges form and the crosshatches represent singular deformations $\boldsymbol{E}^s$ along three fracture lines.

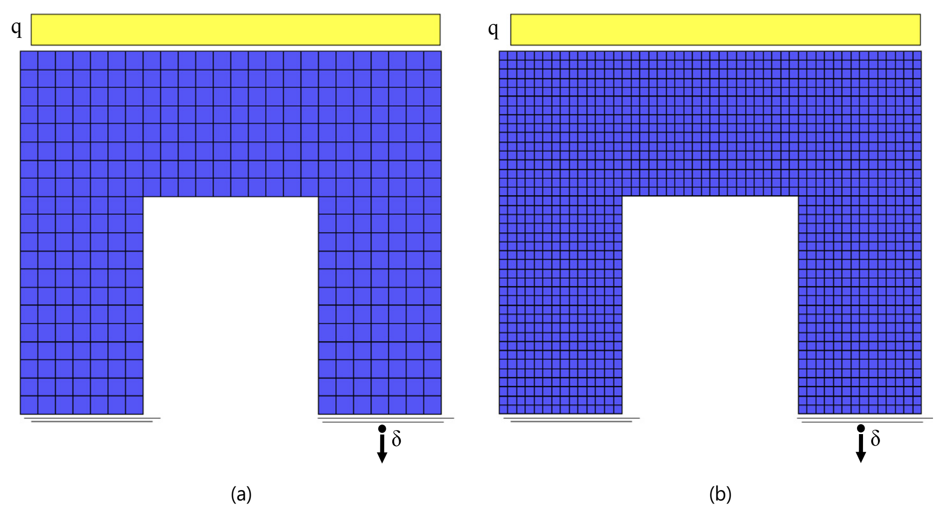

Fig. 20. Two different discretisations of the NRNT portal using 360 (a) and 1140 (b) square elements.

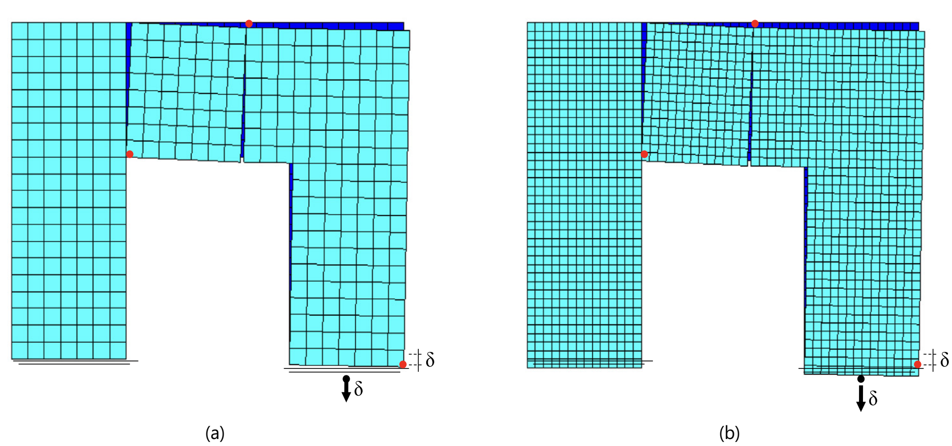

Fig. 21. PRD solutions obtained for the two discretisation of Fig. 20: in both cases, three hinges form and the moving part of the structure becomes isostatic.

form, vertical settlement δ. The non-homogeneous boundary conditions affecting the right support are enforced as follows: denoting $l(\mathrm{A},\mathrm{B})$ a boundary segment lying on the right support, whose ends are A and B, the settling constraint of the right support can be expressed through four restrictions:

$$\mathbf{u}_k(\mathrm{A}) \cdot \mathbf{t} = 0 \quad \mathbf{u}_k(\mathrm{B}) \cdot \mathbf{t} = 0, \tag{42}$$

Table 1
Computational time required to solve the CDF problems as function of the number of planes used to approximate the latent strain cone Sym^{+}.

	Portal with 360 elements (Fig. 22a)		Portal with 1440 elements (Fig. 22b)	
	Constraints [-]	CPU time [s]	Constraints [-]	CPU time [s]
16	55,164	5.63	220,488	822.50
32	107,004	38.21	427,848	2342.21
64	210,684	100.71	842,652	5701.64

$$\mathbf{u}_{\mathrm{k}}(\mathrm{A}) \cdot \mathbf{n} \geq -\delta \quad \mathbf{u}_{\mathrm{k}}(\mathrm{B}) \cdot \mathbf{n} \geq -\delta, \tag{43}$$

$\mathbf{t}$ and $\mathbf{n}$ being the tangent and normal unit vectors along the interface. Restrictions (42, 43) have to be written for each element edge belonging to the right support.

4.3.2. PRD analysis

In this section, we propose the PRD analyses of the NRNT portal of Fig. 19a considering the two different discretisations depicted in Fig. 20. The PRD solutions of the minimum problems are reached

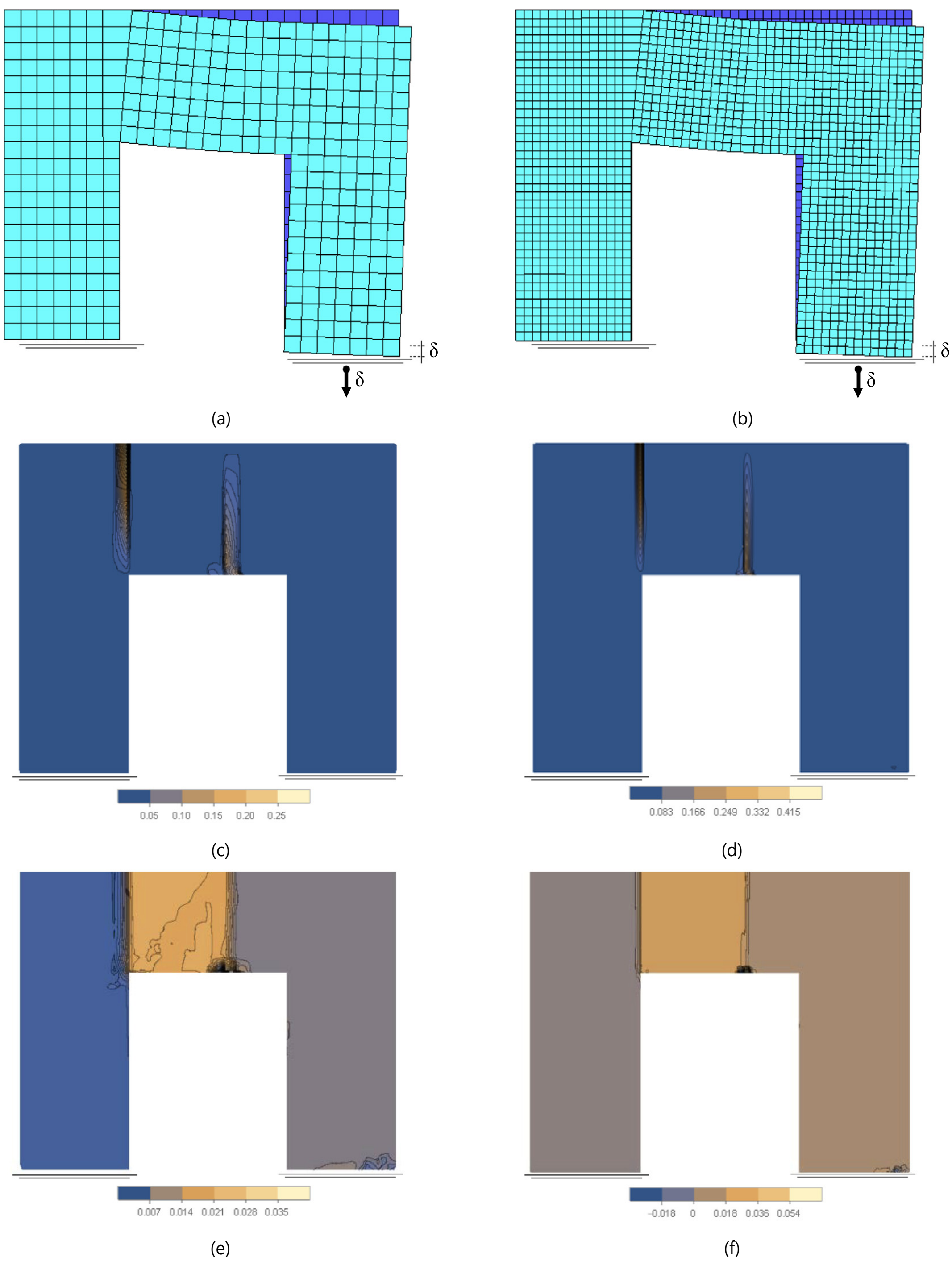

Fig. 22. In (a, b): CDF solutions in terms of displacement fields. In (c, d): contour plot of the field $|\mathbf{E}|^2 = tr\left(\mathbf{E}\mathbf{E}^{\mathrm{T}}\right)$. In (e, f): rotation field over the whole domain.

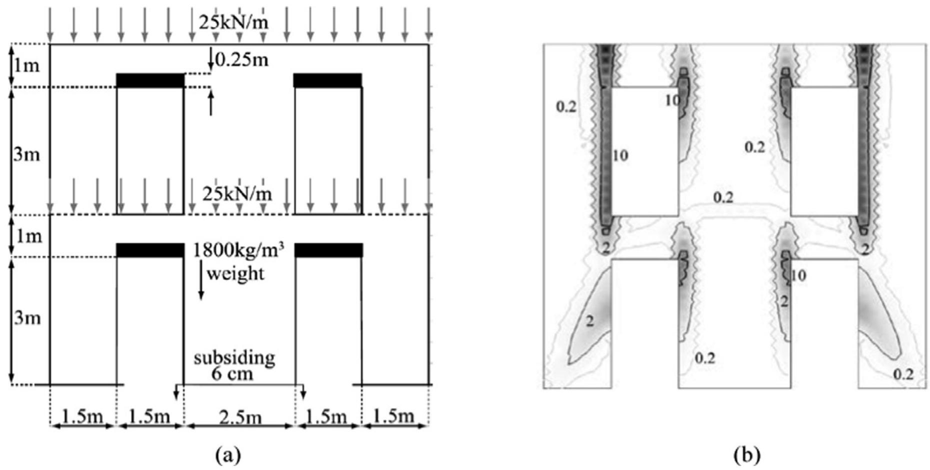

Fig. 23. The two-story, masonry façade studied in [57]: geometry and loads (a); and, contour plot of the maximum plastic strain due to a uniform settlement affecting the inner wall (b).

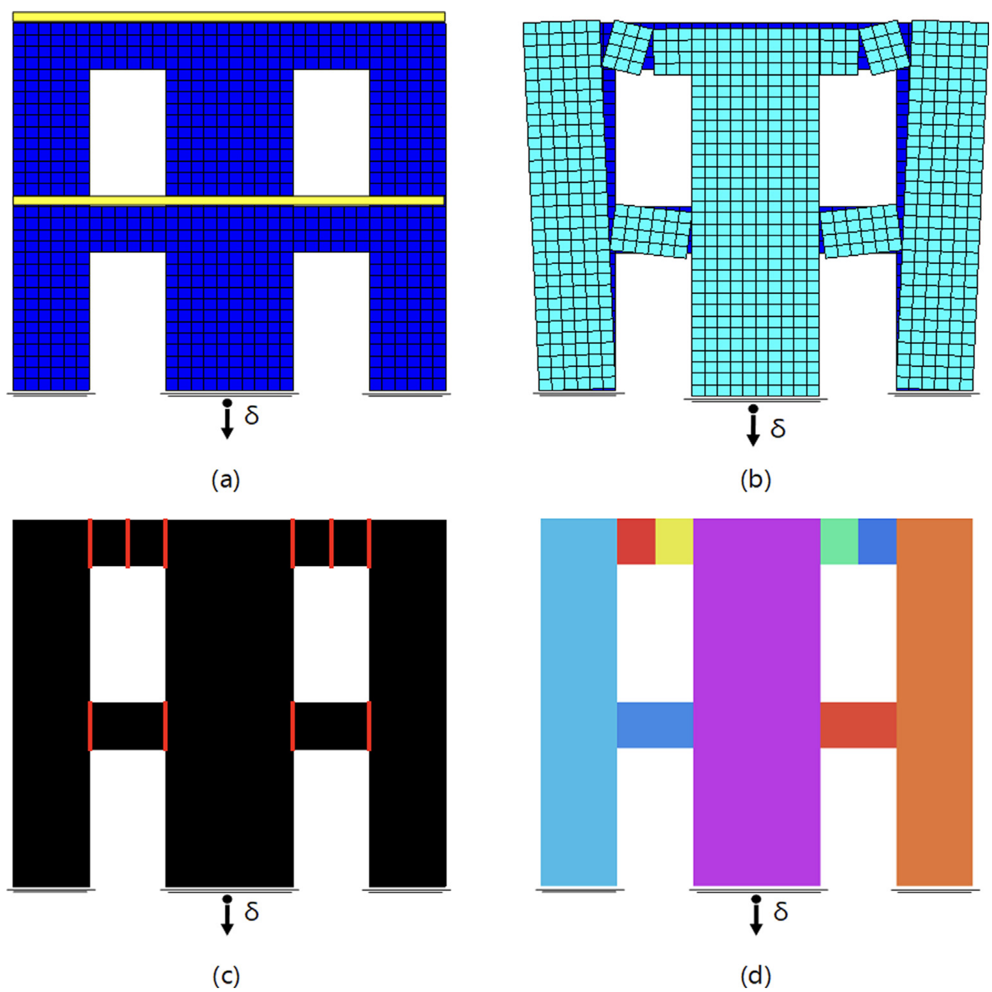

Fig. 24. In (a), the masonry façade of Fig. 23a subjected to a uniform foundation displacement affecting the inner wall. The structure, assumed as composed of NRNT material, is discretized into 800 rigid blocks. In (b), the PRD solution. In (c) the interfaces showing jumps of the displacement field are labelled in red. In (d), the rigid macroblock partition of the structural domain shows nine macroblocks accommodating the foundation displacement. (For interpretation of the references to colour in this figure legend, the reader is referred to the web version of this article.)

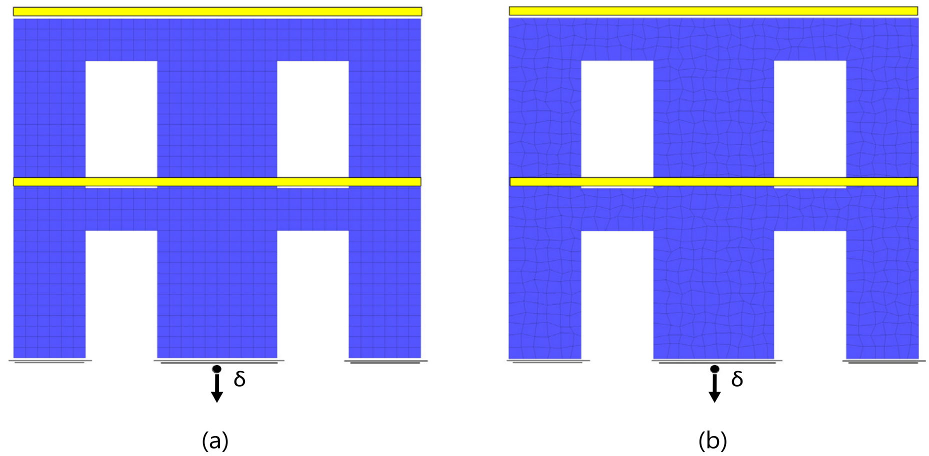

Fig. 25. The masonry façade of Fig. 23a is discretised into 800, 9-node, quadrangular elements and two different FE meshes are considered: structured (a) and unstructured (b).

through the interior point method in 0.06 s and 0.33 s and are reported in Fig. 21.

4.3.3. CDF analysis

In the present section, we illustrate the CDF results of the NRNT portal of Fig. 19 using the two meshes shown in Fig. 20. Particularly, each square element is associated to a 9-node, Lagrangian element. In both cases, the only contribution to the TPE is due to a piecewise uniformly distributed load, besides the use of uniform, isotropic pressure. The CDF problems are solved using different discretisations of the latent strain cone. Particularly, the cone is discretised with 16, 32 and 64 planes. The CDF solutions of the minimum problems are obtained with the interior point and are reported in Table 1. In Fig. 22, the solutions corresponding to 16 planes are reported. The first row of Fig. 22 shows the displacement fields. Fig. 22c-d report the contour plots of $|\mathbf{E}|^2 = tr\left(\mathbf{E}\mathbf{E}^{\mathrm{T}}\right)$ as a measure of the deformation, while Fig. 22e-f show the local rotation fields (i.e. the skew-symmetric part of the displacement field). A denser mesh tends to narrow the non-zero crack regions down.

4.3.4. Discussion

Using the two discretisations, both the PRD and CDF analyses return approximately the same qualitative mechanism. Indeed, looking at the PRD analysis (Fig. 21), a three-hinge mechanism forms and the moving part of the structure becomes statically determined. The PRD mechanism is qualitatively similar to the analytical solution (Fig. 19b). Particularly, looking at the central hinge position, the PRD solution of the discretisation shown in Fig. 21a returns $x/l = 0.70$, while the solution of Fig. 21b returns $x/l = 0.65$. As one can see, by further refining the mesh, the solution approaches the analytical one ($x/l = 0.658$). From Fig. 22a-b, the CDF displacements identify the same mechanism obtained with the PRD method. Moreover, looking at Fig. 22c-d, the deformation gradient is concentrated along two vertical lines, whilst the remaining portion of the structural domain is characterized by strains whose norm is close to zero. It should be noticed that the rotation gradient (Fig. 22e-f) is also essentially concentrated along those two vertical lines and corresponds to a close approximation of the cracks depicted in Fig. 19b. Finer meshes allow to narrow the CDF non-zero strain regions, and thus, to better approximate the fracture pattern. Finally, comparing Fig. 21 and Fig. 22, a good overall concordance amongst the CDF and the PRD solutions can be also observed.

4.4. A masonry façade

In the present section, as a theoretical benchmark, we look at the two-story masonry façade depicted in Fig. 23a. This example is selected from [57], in which an extension of the classic normal, elastic, no-tension (NENT) model was proposed and fully benchmarked against both analytical solutions and experimental cases. In [57] the façade was firstly studied in its undeformed configuration and, then, two different analyses were performed: with the first one, the authors assessed the stability under seismic actions; and, with the second the effects in terms of cracks/stresses due to a uniform foundation settlement affecting the inner pillar were studied. In this section, we focus on the effect of the foundation displacement only.

The geometry of the façade, the loads, and the boundary conditions are represented in Fig. 23a. The structure has a uniform orthogonal depth of 0.50 m and is made up of tuff having a material density ρ = 1800 kg/m^3. Above each opening, a wooden beam with a thickness equal to 0.25 m is present. In the following sections, we address the study of the façade using both the PRD and CDF method.

4.4.1. Numerical solution using a NENT material model

In this section, we briefly recall the results of the analysis performed in [57]. The inner wall of the masonry façade is subjected to a 6 cm, uniform, foundation displacement as shown in Fig. 23a. In Fig. 23b the contour plot of the maximum plastic strain is reported. Looking at that figure, one can notice that the structure shows a peculiar kinematics: the central wall is following the foundation settlement while the lateral walls are rotating outward around their lower external vertices. Because of the presence of the wooden beams above the openings, the lintels do not show any internal fracture and the crack pattern suggests that they rotate rigidly. By computing the mean stress tensor

$$\sigma_m = \frac{1}{\Omega}\left(\int_{\partial\Omega_N} \mathbf{t}\otimes\mathbf{x}\ \mathrm{d}\mathbf{S} + \int_{\Omega} \mathbf{b}\otimes\mathbf{x}\ \mathrm{d}\mathbf{V}\right), \tag{41}$$

it results that the only non-zero component of the mean stress tensor is its vertical component, and, thus the mean stress is σ_{m} =0.176 MPa.

4.4.2. PRD analysis

The masonry façade of Fig. 23a is here analysed modelling the material as NRNT and the BVP is solved through the PRD method. The structure is discretised into 800 square rigid blocks as shown

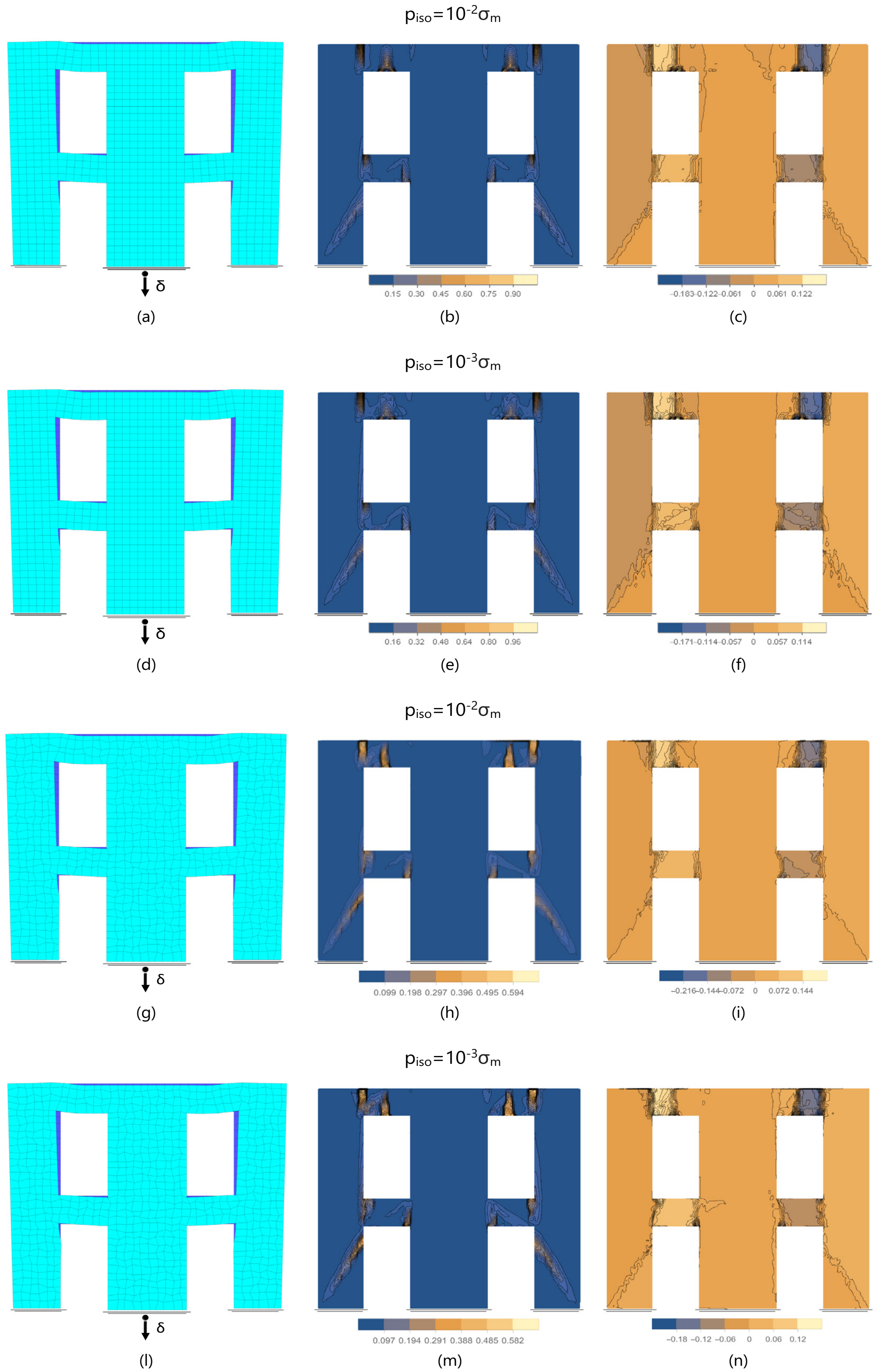

Fig. 26. CDF analyses of the masonry façade of Fig. 23a combining two mesh-discretisations (structured and unstructured) with two isotropic pressure values p_{iso} (i.e. $10^{-2}\sigma_m$ and $10^{-3}\sigma_m$). Particularly, the first two rows correspond to the structured mesh, while the last two to the unstructured mesh. In all cases, the CDF results similar crack patterns. In particular, the bottom part of the external, lateral walls are affected by diagonal cracks.

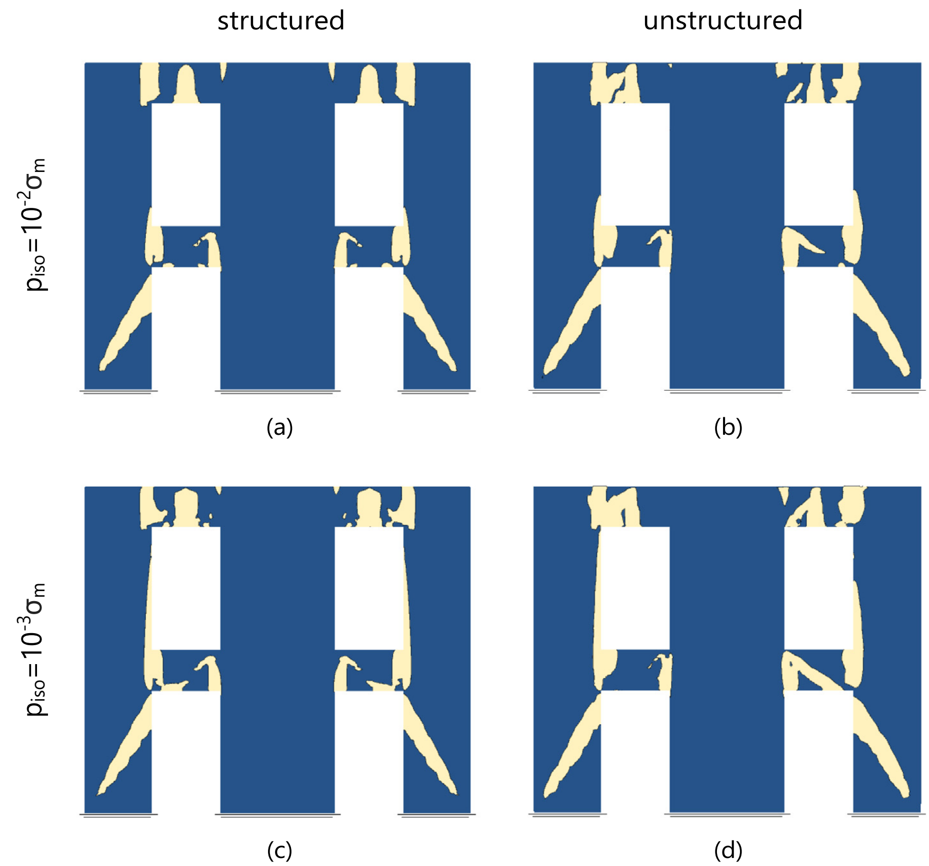

Fig. 27. CDF analyses: the white-regions identify the area where the strain is non-zero (i.e. $|\mathbf{E}|^2 = tr\left(\mathbf{E}\mathbf{E}^{\mathrm{T}}\right)$ is positive).

in Fig. 24a. The vertical loads are represented by rectangular, yellow strips while the self-weight of each block is considered through equivalent, vertical, resultants applied at the centroid. The external walls are considered fixed (i.e. subjected to homogeneous boundary constraints) while the vertical settlement affecting the central wall is enforced using Eqs. (41, 42) with $\delta = 6$ cm. The BVP is graphically summarised in Fig. 24a. The PRD solution is represented in Fig. 24b. It is worth noting that since the wooden beams are not modelled, both the upper lintels are affected by an internal vertical crack. Besides that, the overall kinematics of the façade closely resembles the one obtained with the NENT model and reported in Section 4.4.1. The solution is obtained with the interior point method in 0.25 s (see Fig. 25).

4.4.3. CDF analysis

In this section, to illustrate the influence of both the mesh and the isotropic pressure, we perform four different CDF analyses of the masonry façade of Fig. 23a. Two different FE-discretisations of the structure, both consisting of 800, nine-node, quadrangular elements are considered (see Fig. 25). The first one is based on a *structured* mesh constituted by 9-node Lagrangian FEs having straight and aligned horizontal and vertical edges (Fig. 25a), while the second one is based on an *unstructured* mesh as depicted in Fig. 25b. Specifically, the unstructured mesh is obtained by randomly moving the internal nodes of the structured mesh. Each mesh is analysed considering two values of the isotropic pressurep_{iso}, namely $10^{-2}\sigma_m$ and $10^{-3}\sigma_m$.

As external loads, the action due to secondary structures is taken into account reducing their uniform vertical loads to resultants, which are then applied to the Gauss points of the FEs lying on the bottom part of the rectangular stripes (Fig. 29); in the same way, the self-weight is reduced to concentrated forces applied to the Gauss points of each FE. The constrained boundary is constituted by the bases of the two external walls considered as fixed and by the base of the internal wall that is subjected to a unilateral vertical displacement δ equal to 6 cm. Therefore, the external bases are subjected to homogeneous boundary conditions, while on the internal one the vertical foundation displacement is still enforced using Eqs. (41, 42) as already assumed for the PRD analysis (**Section 4.4.2**).

In Fig. 26 the results of the four CDF analyses combining the two mesh-discretisations with the two isotropic pressure values are reported. In all cases, the solutions are obtained with the interior point method and the calculation time is in average about 60 s (see Table 1).

Specifically, as done in the previous cases, the fractures, represented by the latent strain field $\mathbf{E}$, are graphically showed in the second column through the contour plot of $|\mathbf{E}|^2 = tr\left(\mathbf{E}\mathbf{E}^{\mathrm{T}}\right)$. Even in the present case, the gradient of deformation is concentrated along some narrow bands, whilst the remaining portion of the structural domain is characterized by strains whose norm is close to zero. The rotation field (i.e. the skew-symmetric part of the displacement field) corresponding to these four distinct analyses is depicted along the third column of Fig. 26. The solution in terms

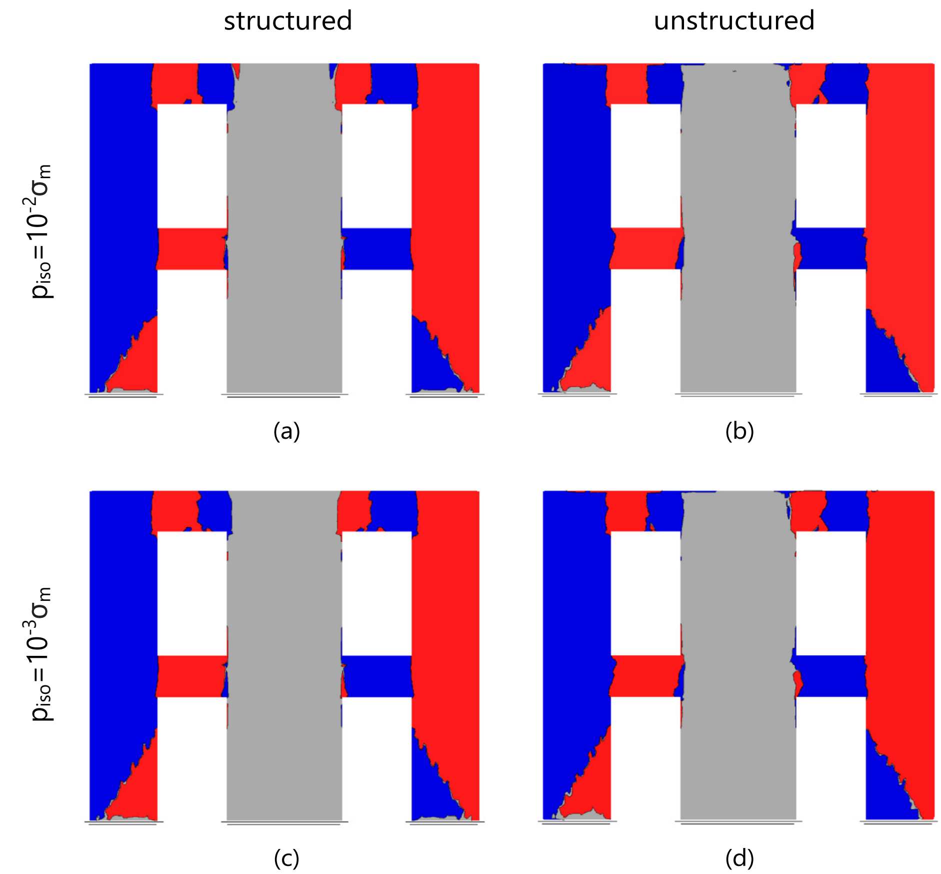

Fig. 28. The CDF rigid macroblock partition can be clearly highlighted by labelling positive and negative rotations in red and blue, respectively. (For interpretation of the references to colour in this figure legend, the reader is referred to the web version of this article.)

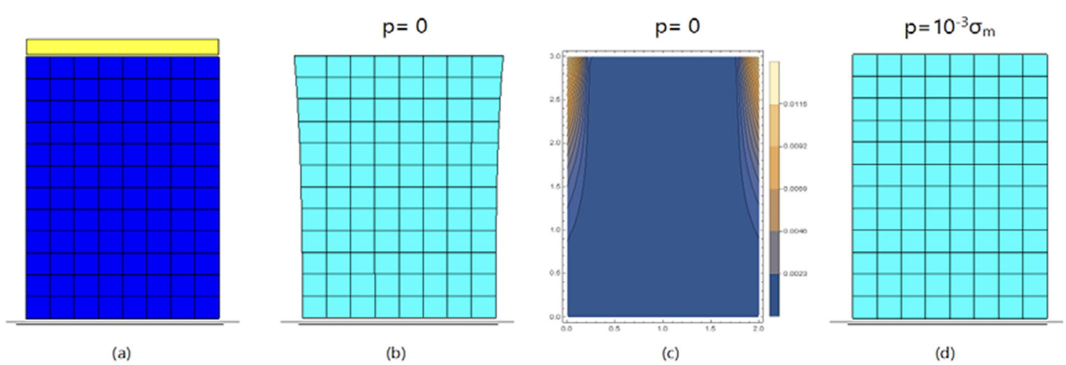

Fig. 29. Effect of the isotropic pressure. An NRNT panel loaded on the top edge and whose base is fixed (a). In (b) the CDF solution without any isotropic pressure shows a non-zero displacement filed whose contribution to the total potential energy is zero (b, c). As a small value of the isotropic pressure is assumed, the displacement becomes zero everywhere, as expected (d).

of rotation field is consistent with the solution in terms of fractures/strains.

4.4.4. Comparison

Both the PRD and CDF analyses return solutions coherent and consistent with a study proposed and benchmarked in [57], where a NENT material was adopted. In particular, comparing the crack patterns, the PRD and CDF solutions return qualitatively the same fracture mechanism shown in [57] (the reader is referred to Fig. 23b showing the contour plot of the maximum plastic strain). In all cases, the mechanism is the same: the central wall is following the foundation settlement while the lateral walls are rotating outward around their lower external vertices. The only discrepancy amongst both the PRD and CDF analyses and the one proposed in [57] regards the fractures involving the upper lintels, as in [57] the NENT model they were modelled as wooden beams.

5. Discussions

In the present section, we discuss the CDF peculiarities with respect to the PRD method referring to the case study illustrated in **Section 4.4**. Looking at the CDF analyses shown in Fig. 26, the primary outcome is that the results are independent of both the discretisation and the isotropic pressure. Indeed, either using a structured mesh or a unstructured one, the CDF method returns

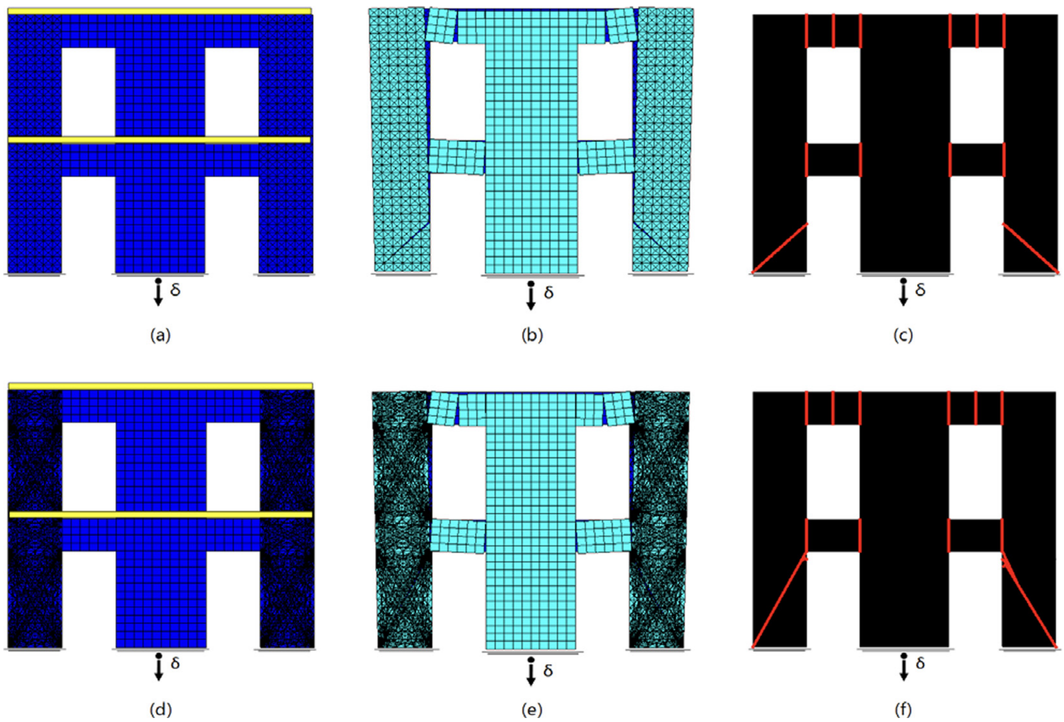

Fig. 30. In (a-c), PRD analysis of the masonry façade of Fig. 23a where the external walls are discretised using triangles. With this new discretisation, the outer walls show two slanted cracks which were not present in the results reported in Fig. 24. In (d-e), a ground structure-like discretisation of the external walls: the crack pattern is the same obtained with the CDF method.

the same crack pattern. Moreover, different, small values of the isotropic pressure do not affect the results. Indeed, even with a very small value of the isotropic pressure ($10^{-3}\sigma_m$), the CDF solutions (second and fourth row of Fig. 26) are in a good agreement with the one obtained with the NENT model [57]. This aspect is further highlighted in Fig. 27 and Fig. 28, where the structural macroblock partition defined by the CDF analyses is clearly visible.

The use of a fictitious isotropic pressure directly comes from the so-called **Safe Load condition** (Remark 3). Without such negligible confinement, the energy is not coercive, meaning that the displacement can grow indefinitely at zero energy price. In our model, this kind of confinement is imposed by adding all over the loaded (i.e. non-constrained) boundary a given uniform pressure of very small magnitude compared to the working mean stress (its value is some orders of magnitude less than the atmospheric pressure). Such fictitious confinement can be seen as an indirect way to allow for a small cohesion into the material. Therefore, its use has also the effect of encouraging rigid block mechanisms (i.e. concentrated fractures) over diffuse deformations. In this sense, its use provides the BVP with the **Safe Load Condition**. This aspect can be clearly illustrated with the following example. Let us consider an NRNT panel loaded on the top edge by a uniform distributed load and whose horizontal lower edge is fixed (Fig. 29). The CDF analysis returns the solution depicted in Fig. 29b (scaled up for the sake of clarity). The external upper parts of the panel show an outward displacement: the Gauss points of the blocks can freely move since their contribution to the total potential energy is zero. And, this is even more clear by looking at Fig. 29c. Once an isotropic pressure along the external boundary is added as a small fraction of the mean stress ($10^{-3}\sigma_m$), the solution becomes precisely the one we expect in a real wall (Fig. 29d), that is the displacement field is zero everywhere.

The main difference among PRD and CDF approaches can be appreciated looking at Fig. 24 and Fig. 27. All CDF analyses show two specular, diagonal cracks on the lower parts of the external

Table 3
Computational burden for the PRD analyses.

Masonry Façade	Elements [-]	Constraints [-]	CPU time [s]
Quad elements (Fig. 24)	800	5,984	0.25
Quad and triangles elements (Fig. 30a)	1,952	12,128	0.51
Ground structure-type discretisation (Fig. 30d)	19,884	119,728	30.1

Table 2
Computational time required to solve the CDF problems.

Masonry Façade	Elements [-]	p_{iso} [-]	Constraints [-]	CPU time [s]
Structured	800	$10^{-3}\sigma_m$	468,132	56.45
Unstructured	800	$10^{-3}\sigma_m$	468,132	90.25
Structured	800	$10^{-2}\sigma_m$	468,132	52.72
Unstructured	800	$10^{-2}\sigma_m$	468,132	82.32

walls due to the walls' outward rotation: this is a peculiar fracture pattern for a non-fully-activated masonry wall [89]. However, the PRD analyses do not show any diagonal crack on those external walls. This aspect is the direct consequence of what illustrated in Section 4.2, i.e. the mesh-dependency of the PRD approach. Indeed, if we consider a different discretisation such as the one reported in Fig. 30a, the PRD analysis returns the mechanism depicted in Fig. 30b, which also shows two diagonal cracks affecting the outer walls as highlighted in Fig. 30c. However, such diagonal cracks are not aligned with the ones predicted by the CDF analyses. A way to overcome the intrinsic mesh dependency of the PRD method is to consider a ground structure-like discretisation of the walls as shown in Fig. 30d. Additional numerical possibilities to overcome the mesh dependency can be found in [62,90]. Specifically, the masonry panels are discretised connecting all nodes lying on their boundaries. In such a way, the PRD discretisation is enriched with a large number of internal interfaces, and thus of possible crack lines. The corresponding PRD results are reported in Fig. 30e-f: in the present case, the crack pattern is similar to the CDF one.

Tables 2 and 3 show the computational time required to solve the masonry façade problem using the CDF and the PRD method, respectively. As the numbers of element are the same, all CDF problems involve 468,132 linear constraints. This large number is due to the fine level of discretisation of the semidefinite positive strain cone (64 planes). The use of 32 or even 16 planes provides still a good approximation of the strain cone, while reducing significantly the computational time (see Table 1). We point out that in the case of the masonry façade, the computational time in average required to solve the problem is much lower than the one needed for the CDF analyses of the portals of Section 4.3.3. Under a numerical perspective, the differences among the masonry façade and the simple portal with the finer mesh (Fig. 22b) is the number of elements (almost doubled in the simple portal) and the self-weight that was not considered in the CDF analyses of Section 4.3.3.

We point out again that for masonry-like unilateral materials extensional deformations (i.e. fractures), are allowed at zero energy price, and can be either regular or singular. Specifically, extensional deformation can appear either as diffuse (*smeared cracks*) or as concentrated (*macroscopic cracks*), and, on an energy ground, there is not any reason to prefer one to another. For real masonry structures, the fact that rigid block deformation seems to be the preferred failure mode stems from mechanical characteristics, such as toughness, interlocking, finite friction and cohesion. These mechanical characteristics are not inherent to the simplified NRNT continuum model. For this reason, once the CDF analysis is coupled with a small value of the isotropic pressure, it can adequately reproduce this phenomenological behaviour. Conversely, this aspect is implicitly taken into account by the PRD method because of the piecewise rigidity assumption on the displacement field.

6. Conclusions

In the present paper, we proposed the Continuous Displacement for Fracture (CDF) method, a new continuous energy-based numerical approach for the analyses of masonry structures. The structure is modelled through the NRNT material models, i.e. as a continuum composed of unilateral material, perfectly rigid in compression and soft in tension, suffering small strains. The solution of the boundary value problem is obtained minimising the total potential energy in the space of continuous displacements. Independently of the adopted mesh, CDF allows to predict the fracture pattern produced by a given set of load and kinematical data (e.g. settlements, distortions). The CDF performances were illustrated and compared in detail against both analytical solutions and an opposite energy-based strategy, i.e. the PRD method that minimises the total potential energy in the space of small piecewise rigid displacement fields.

The CDF approach is based on a classical finite element (FE) mesh description of the structural domain where the nodal displacements are continuous. In this case, strain cannot be singular and fractures appear as *smeared*; narrow bands (which may even cross single elements) where high strains are present can be detected and, most importantly, such bands can also cross single elements, meaning that they are not restricted to lie on the element boundaries, as in common rigid block models.

As the PRD method, CDF uses displacements as primal unknowns, and in this sense, it allows a direct control of the main variables, particularly for problems regarding masonry structures in which the cracks are induced by settlements. Moreover, as it is energy-based, the CDF method offers a consistent and robust way to solve the BVP through a Linear Programming problem, allowing for an efficient and relatively fast computational solving. Indeed, all CDF analyses were performed using a very fine discretisation of the latent strain cone (i.e. 64 planes). To further reduce the computational time and to still have an adequate cone approximation, a lower number of planes can be used as shown in Section 4.3.3 and in Table 1. As outcomes of the in-depth comparison among the CDF and PRD methods, a few important differences should be highlighted:

- the PRD method is a "natural" linear minimization problem; the CDF method, to become a linear programming formulation, requires a linearization of a quadratic condition;
- the CDF method is numerically more cumbersome because of the large number of constraints coming from the above linearization and because of the finer mesh required to approximate large displacement gradients;
- with the CDF method, the macro-block partition of the structural domain may be encouraged by applying, all over the loaded boundary, a fictitious, small uniform pressure (**Safe Load condition**). We showed that this value can be a small fraction of the mean working, compressive stress, and it is two orders of magnitude less than the atmospheric pressure;
- in some cases, numerical solutions obtained with the PRD method cannot converge to exact cracks which are not parallel to the skeleton of the mesh. Therefore, even if the gross subdivision into macro-blocks predicted by the PRD method is usually consistent with the exact one (that is one corresponding to a weak minimum of the energy), the fine details of the exact interfaces among blocks are lost. A way to overcome the PRD mesh dependency is to consider ground structure-type discretisation as shown in Fig. 30d. Conversely, such fine details are instead accurately detected by approximate solutions obtained via the CDF method; and,
- in practical applications, the main critical issue of a fracture survey is identifying the precise cause of the disarrangements and distortions, which are detectable on the surface of the construction. That is, performing an inverse-analysis to identify the particular form of foundation settlements producing the detected crack pattern. In this respect, the PRD method, as it is much faster than CDF, constitutes the preferential approach for inverse settlements induced crack problems as these analyses require a huge number of numerical solutions to accurately reproduce the detected fracture pattern [33].

The main outcome of using CDF to solve the BVP for NRNT material is that it perfectly captures rigid macro-block mechanisms exhibited by masonry structures when subjected to severe external environment changes. And, more importantly, CDF does not suffer of mesh dependency in locating cracks. Therefore, CDF represents a robust computational, energy-, displacement-based tool to solve typical problems for assessing masonry structures.

Declaration of Competing Interest

The authors declare that they have no known competing financial interests or personal relationships that could have appeared to influence the work reported in this paper.

References

[1] Gilbert M, Melbourne C. Rigid-block analysis of masonry structures. Struct Eng 1994;72(21).
[2] Gilbert M, Casapulla C, Ahmed HM. Limit analysis of masonry block structures with non-associative frictional joints using linear programming. Comput Struct 2006;84(13–14):873–87.
[3] Portioli F, Casapulla C, Gilbert M, Cascini L. Limit analysis of 3D masonry block structures with non-associative frictional joints using cone programming. Comput Struct 2014;143:108–21.
[4] D'Ayala D, Casapulla C. Limit state analysis of hemispherical domes with finite friction. Historical constructions, possibilities of numerical and experimental techniques; 2001. p. 617–26.
[5] Orduña A, Lourenço PB. Three-dimensional limit analysis of rigid blocks assemblages. Part I: Torsion failure on frictional interfaces and limit analysis formulation. Int J Solids Struct 2005;42(18–19):5140–60.
[6] Livesley R. Limit analysis of structures formed from rigid blocks. Int J Numer Meth Eng 1978;12(12):1853–71.
[7] Lourenço PB, Rots JG. Multisurface interface model for analysis of masonry structures. J Eng Mech 1997;123(7):660–8.
[8] Baggio C, Trovalusci P. Discrete models for jointed block masonry walls. In The Sixth North American Masonry Conference, vol. 2. 1993; pp. 939–49.
[9] Zampieri P, Zanini MA, Faleschini F, Hofer L, Pellegrino C. Failure analysis of masonry arch bridges subject to local pier scour. Eng Fail Anal 2017;79:371–84.
[10] Reccia E, Milani G, Cecchi A, Tralli A. Full 3D homogenization approach to investigate the behavior of masonry arch bridges: The Venice trans-lagoon railway bridge. Constr Build Mater 2014;66:567–86.
[11] Lemos JV. Discrete element modeling of masonry structures. Int J Archit Herit 2007;1(2):190–213.
[12] Tóth A, Orbán Z, Bagi K. Discrete element analysis of a stone masonry arch. Mech Res Commun 2009;36(4):469–80.
[13] Simon J, Bagi K. Discrete element analysis of the minimum thickness of oval masonry domes. Int J Architectural Heritage 2016;10(4):457–75.
[14] Sarhosis V, Bagi K, Lemos J, MG. Computational modeling of masonry structures using the discrete element method. IGI Global; 2016.
[15] Forgács T, Sarhosis V, Bagi K. Minimum thickness of semi-circular skewed masonry arches. Eng Struct 2017;140:317–36.
[16] Van Mele T, McInerney J, DeJong MJ, Block P. Physical and computational discrete modeling of masonry vault collapse. Structural analysis of historical constructions: proceedings of the 8th International Conference on Structural Analysis of Historical Constructions, SAHC 2012, 15-17 October, Wroclaw, Poland, pp. 2252-2560,DWE; 2012.
[17] McInerney J, DeJong MJ. Discrete element modeling of groin vault displacement capacity. Int J Architectural Heritage 2015;9(8):1037–49.
[18] Meriggi P, de Felice G, De Santis S, Gobbin F, Mordanova A, Pantò B. Distinct element modelling of masonry walls under out-of-plane seismic loading. Int J Architectural Heritage 2019;13(7):1110–23.
[19] Gobbin F, de Felice G, Lemos JV. A discrete element model for masonry vaults strengthened with externally bonded reinforcement. Int J Architectural Heritage 2020:1–14.
[20] Moreau JJ. On unilateral constraints, friction and plasticity. In in "New Variational Techniques in Mathematical Physics"(G. Capriz and G. Stampacchia, Ed.). CIME ciclo Bressanone; 1973.
[21] Como M. Statics of historic masonry constructions. Berlin: Springer; 2013.
[22] Danyzy AAH. Méthode générale pour déterminer la résistance qu'il faut opposer à la poussée des voûtes. Histoire de la Société Royale des Sciences établie à Montpellier, Vols. 2(1718-1745), pp. 40-56. Published : Lyon 1778, 1732.
[23] Frézier AF. La théorie et la pratique de la coupe de pierres et des bois pour la construction des voûtes et autres parties des bâtiments civils et militaires, ou traité de stéréotomie à l'usage de l'architecture (3 vols), Strasbourg/Paris, 1737-39.
[24] Acikgoz S, Soga K, Woodhams J. Evaluation of the response of a vaulted masonry structure to differential settlements using point cloud data and limit analyses. Constr Build Mater 2017;150:916–31.
[25] D'Altri AM, De Miranda S, Castellazzi G, Sarhosis V, Hudson J, Theodossopoulos D. "Historic barrel vaults undergoing differential settlements". Int J Architectural Heritage 2019:1–14.
[26] Pepe M, Sangirardi M, Reccia E, Pingaro M, Trovalusci P, de Felice G. Discrete and continuous approaches for the failure analysis of masonry structures subjected to settlements. Front Built Environ 2020;6(43).
[27] Sangirardi M, Malena M, de Felice G. Settlement induced crack pattern prediction through the jointed masonry model; 2019.
[28] Spada A. The effect of vertical ground movement on masonry walls simulated through an elastic–plastic interphase meso-model: a case study. Arch Appl Mech 2019;89(8):1655–76.
[29] DeJong MJ. Settlement effects on masonry structures. In: Proceedings of the 10th international conference on structural analysis of historical constructions, SAHC 2016. p. 449–56.
[30] Portioli F, Cascini L. Large displacement analysis of dry-jointed masonry structures subjected to settlements using rigid block modelling. Eng Struct 2017;148:485–96.
[31] Heyman J. The stone skeleton. Int J Solids Struct 1966;2(2):249–79.
[32] Angelillo M. Practical applications of unilateral models to Masonry Equilibrium. In: Angelillo M, editor. Mechanics of Masonry Structures. Vienna: Springer; 2014. p. 109–210.
[33] Kooharian A. Limit analysis of voussoir (segmental) and concrete archs. J Am Concr Inst 1952;24(4):317–28.
[34] Como M. On the equilibrium and collapse of masonry structures. Meccanica 1992;27(3):185–94.
[35] Angelillo M. Static analysis of a Guastavino helical stair as a layered masonry shell. Compos Struct 2015;119:298–304.
[36] Angelillo M, Olivieri C, DeJong MJ. A new equilibrium solution for masonry spiral stairs. Eng Struct 2021;238:112176.
[37] Angelillo M, Babilio E, Fortunato A. Singular stress fields for masonry-like vaults. Continuum Mech Thermodyn 2013;25(2–4):423–41.
[38] Angelillo M, Fortunato A, Montanino A, Lippiello M. Singular stress fields in masonry structures: Derand was right. Meccanica 2014;49(5):1243–62.
[39] Angelillo M, Fortunato A, Gesualdo A, Iannuzzo A, Zuccaro G. Rigid block models for masonry structures. Int J Masonry Res Innovation 2018;3 (4):349–68.
[40] Block P. Thrust network analysis: exploring three-dimensional equilibrium, Doctoral dissertation. Massachusetts Institute of Technology 2009.
[41] Block P, Ciblac T, Ochsendorf JA. Real-time limit analysis of vaulted masonry buildings. Comput Struct 2006;84(29–30):1841–52.
[42] Block P, Ochsendorf JA. Thrust network analysis: A new methodology for three-dimensional equilibrium. J Int Assoc Shell Spatial Struct 2007;48 (3):167–73.
[43] Block P, Lachauer L. Three-dimensional funicular analysis of masonry vaults. Mech Res Commun 2014;56:53–60.
[44] Coccia S, Como M, Di Carlo F. Wind strength of gothic cathedrals. Eng Fail Anal 2015;55:1–25.
[45] Coccia S, Di Carlo F, Rinaldi Z. Collapse displacements for a mechanism of spreading-induced supports in a masonry arch. Int J Adv Struct Eng 2015;7 (3):307–20.
[46] Fortunato A, Fabbrocino F, Angelillo M, Fraternali F. Limit analysis of masonry structures with free discontinuities. Meccanica 2018;53(7):1793–802.
[47] Gesualdo A, Cennamo C, Fortunato A, Frunzio G, Monaco M, Angelillo M. Equilibrium formulation of masonry helical stairs. Meccanica 2017;52 (8):1963–74.
[48] Gesualdo A, Brandonisio G, De Luca A, Iannuzzo A, Montanino A, Olivieri C. Limit analysis of cloister vaults: the case study of Palazzo Caracciolo di Avellino. J Mech Mater Struct 2019;14(5):739–50.
[49] Huerta S. Galileo was wrong: the geometrical design of masonry arches. Nexus Netw J 2006;8(2):25–52.
[50] Huerta S. Geometry and equilibrium: The gothic theory of structural design. Struct Eng 2006;84(2):23–8.
[51] Huerta S. The analysis of masonry architecture: a historical approach: to the memory of professor Henry J. Cowan. Architectural Sci Rev 2008;51 (4):297–328.
[52] Ochsendorf JA. Collapse of masonry structures Doctoral dissertation:. University of Cambridge; 2002.
[53] Ochsendorf J. The masonry arch on spreading supports. Struct Eng 2006;84 (2):29–34.
[54] Zampieri P, Amoroso M, Pellegrino C. The masonry buttressed arch on spreading support. Structures 2019;20:226–36.
[55] Giuffrè A. Letture sulla Meccanica delle Murature Storiche. Edizioni Kappa 1991.
[56] Lucchesi M, Padovani C, Zani N. Masonry-like solids with bounded compressive strength. Int J Solids Struct 1996;33(14):1961–94.
[57] Angelillo M, Cardamone L, Fortunato A. A numerical model for masonry-like structures. J Mech Mater Struct 2010;5(4):583–615.
[58] Marfia S, Sacco E. Numerical procedure for elasto-plastic no-tension model. Int J Comput Methods Eng Sci Mech 2005;6(3):187–99.
[59] Iannuzzo A, Angelillo M, De Chiara E, De Guglielmo F, De Serio F, Ribera F, et al. Modelling the cracks produced by settlements in masonry structures. Meccanica 2018;53(7):1857–73.
[60] Iannuzzo A. A new rigid block model for masonry structures. PhD Dissertation, Università degli Studi di Napoli Federico II; 2017.
[61] Tralli A, Chiozzi A, Grillanda N, Milani G. Masonry structures in the presence of foundation settlements and unilateral contact problems. Int J Solids Struct 2020;191:187–201.
[62] Tiberti S, Grillanda N, Mallardo V, Milani G. A Genetic Algorithm adaptive homogeneous approach for evaluating settlement-induced cracks in masonry walls. Eng Struct 2020;221:111073.
[63] Angelillo M, Babilio E, Fortunato A. Numerical solutions for crack growth based on the variational theory of fracture. Comput Mech 2012;50(3):285–301.
[64] Gesualdo A, Monaco M. Constitutive behaviour of quasi-brittle materials with anisotropic friction. Latin Am J Solids Struct 2015;12(4):695–710.

[65] Angelillo M, Babilio E, Fortunato A, Lippiello M, Montanino A. Analytic solutions for the stress field in static sandpiles. Mech Mater 2016;95:192–203.
[66] De Serio F, Angelillo M, Gesualdo A, Iannuzzo A, Zuccaro G, Pasquino M. Masonry structures made of monolithic blocks with an application to spiral stairs. Meccanica 2016;53(8):2171–91.
[67] Milani G, LPB. 3D non-linear behavior of masonry arch bridges. Comput Struct, 110; 2012. p. 133–50.
[68] Chiozzi A, Milani G, Tralli A. A Genetic Algorithm NURBS-based new approach for fast kinematic limit analysis of masonry vaults. Comput Struct 2017;182:187–204.
[69] Bertolesi E, Milani G, Lourenço PB. Implementation and validation of a total displacement non-linear homogenization approach for in-plane loaded masonry. Comput Struct 2016;176:13–33.
[70] Iannuzzo A, Van Mele T, Block P. Piecewise Rigid Displacement (PRD) method: A limit analysis-based approach to detect mechanisms and internal forces through two dual energy criteria. Mech Res Commun 2020;107:103557. https://doi.org/10.1016/j.mechrescom.2020.103557.
[71] Iannuzzo A, Dell'Endice A, Van Mele T, Block P. Numerical Limit Analysis-based modelling of masonry structures subjected to large displacements. Comput Struct 2020;242:106372.
[72] Giaquinta M, Giusti E. Researches on the equilibrium of masonry structures. Arch Ration Mech Anal 1985;88(4):359–92.
[73] Anzellotti G. A class of convex non-coercive functionals and masonry-like materials. Annales de l'IHP Analyse non linéaire 1985;2(4):261–307.
[74] Angelillo M, Fortunato A. "Equilibrium of masonry vaults," Lecture Notes in Applied and Computational Mechanics. Novel approaches in civil engineering (Eds Fremond M, Maceri F) 2004;14:105–11.
[75] Fortunato A, Babilio E, Lippiello M, Gesualdo A, Angelillo M. Limit analysis for unilateral masonry-like structures. Open Constr Build Technol J 2016;10(Suppl 2:M12):346–62.
[76] Ambrosio L, Fusco N, Pallara D. Functions of bounded variation and free discontinuity problems. Oxford, UK: Clarendon Press; 2000.
[77] Tabbakhha M, Modaressi-Farahmand-Razavi A. Analyzing the effect of workmanship quality on performance of unreinforced masonry walls through numerical methods. Comput Struct 2016;167:1–14.
[78] Moseley H. On a new principle in statics, called the Principle of least Pressure. The London, Edinburgh, and Dublin Philosophical Magazine and J Sci 1833;3(16):285–8.
[79] Dantzig G, Orden A, Wolfe P. The generalized simplex method for minimizing a linear form under linear inequality restraints. Pac J Math 1955;5(2):183–95.
[80] Mehrotra S. On the implementation of a primal-dual interior point method. SIAM J Optim 1992;2(4):575–601.
[81] Vanderbei R. Linear programming. Springer; 2015.
[82] Dantzig G. Linear programming and extensions. Princeton University Press; 2016.
[83] Bathe K, Wilson E. Numerical methods in finite element analysis, Englewood Cliffs, NJ. USA: Prentice-Hall; 1976.
[84] Szabó B, Babuška I. Finite element analysis, New York, NY, USA; 1991.
[85] Wolfram S. The Mathematica Book, 5th ed., Wolfram Media; 2003.
[86] Cplex II. V12. 1: User's Manual for CPLEX. International Business Machines Corporation, Vols. 46(53), 157; 2009.
[87] Iannuzzo A. Energy based fracture identification in masonry structures: the case study of the church of "Pietà dei Turchini". J Mech Mater Struct 2019;14(5):683–702.
[88] Bagi K. When Heyman's Safe Theorem of rigid block systems fails: Non-Heymanian collapse modes of masonry structures. Int J Solids Struct 2014;51(14):2696–705.
[89] De Lorenzis L, Dimitri R, Ochsendorf J. Structural study of masonry buttresses: the stepped form. Proc Inst Civil Eng-Struct Build 2012;165:499–521.
[90] Milani G. Upper bound sequential linear programming mesh adaptation scheme for collapse analysis of masonry vaults. Adv Eng Softw 2015;79:91–110. https://doi.org/10.1016/j.advengsoft.2014.09.004.
[91] Olivieri C, Angelillo M, Iannuzzo A, Fortunato A. Parametric design of purely compressed shells. Mechanics of Materials 2021;155:103782.